Ore Geology Reviews 164 (2024) 105847

Contents lists available at ScienceDirect

Ore Geology Reviews

journal homepage: www.elsevier.com/locate/oregeorev

Genesis and supergene weathering of tetrahedrite-(Hg) in *meta*-carbonate rocks: Bearing on differential mobility of priority pollutant metals

Massimo D'Orazio [a,*], Cristian Biagioni [a], Paolo Fulignati [a], Anna Gioncada [a], Jiří Sejkora [b,c], Zdeněk Dolníček [b]

[a] Dipartimento di Scienze della Terra, Università di Pisa, Via S. Maria 53, I-56126 Pisa, Italy
[b] Department of Mineralogy and Petrology, National Museum, Cirkusová 1740, CZ-19300 Prague 9, Czech Republic
[c] Earth Sciences Institute, v.v.i., Slovak Academy of Sciences, Dúbravská cesta 9, SK-840 05 Bratislava, Slovakia

ARTICLE INFO

Keywords:
Tetrahedrite-(Hg)
Cinnabar
Mercury
Supergene alteration
Element mobility
Priority pollutant metal

ABSTRACT

The Cu-Sb-Hg mineralization of San Giuliano Terme (Monti Pisani, Tuscany, Italy) is characterized by the widespread occurrence of deeply altered tetrahedrite-(Hg) hosted within joints and faults in the Liassic "Calcari ceroidi" Formation. Through a multi-technique approach (optical and scanning electron microscopy, electron microprobe analysis, single-crystal and powder X-ray diffraction, micro-Raman spectroscopy, X-ray fluorescence, fluid inclusion analysis), tetrahedrite-(Hg) and its alteration products have been characterized and data about its genesis and successive supergene weathering have been collected. Tetrahedrite-(Hg) from San Giuliano Terme has the empirical formula $Cu_{9.92}Ag_{0.02}(Hg_{1.64}Fe_{0.30}Zn_{0.04})_{\Sigma 1.98}(Sb_{3.53}As_{0.56})_{\Sigma 4.09}S_{12.95}$, and is found with scarce gangue minerals represented by calcite, baryte, and very rare fluorite. The mineralization formed from hydrothermal fluids with moderately high salinity (~17.5 wt% $NaCl_{equiv.}$) of dominantly metamorphic origin at T ~ 285 °C. Tetrahedrite-(Hg) is usually fully replaced by a mixture of cinnabar, roméite-group minerals, malachite, and rarely azurite. Based on the modal abundance of the mineralogical constituents and their micro-textures, four stages of supergene weathering of tetrahedrite-(Hg) have been recognized. The alteration stages reflect the progressive ingression of meteoric water into the system, with consequent oxidation of tetrahedrite-(Hg) and the introduction of Ca^{2+}, HCO_3^- and H_2O, as well as the progressive removal of S, Sb, and Cu. The relative proportions of the supergene minerals in the four alteration stages can be taken as a proxy for the mobility of the main chemical constituents of tetrahedrite-(Hg), three of which (Hg, Sb, and Cu) are priority pollutant metals. Mercury was found to be the least mobile element in the reconstructed geochemical process. In fact, the widespread precipitation of cinnabar in the space formerly occupied by tetrahedrite-(Hg) hinders the dispersion of Hg in the environment, sequestering it in a solid matrix.

1. Introduction

Tetrahedrite group minerals (hereafter TGMs) form one of the most complex isotypic series of chalcogenosalts typically occurring in hydrothermal ore deposits. Their general formula is $^{M(2)}A_6{}^{M(1)}(B_4C_2)^{X(3)}D_4^{S(1)}Y_{12}^{S(2)}Z$, where the capital letters indicate different chemical constituents and the superscripts the different structural sites (Biagioni et al., 2020a). Among the more than 35 different species currently known, the most common ones belong to the sulfosalt series of tetrahedrite and tennantite. Both have Cu as the dominant A and B chemical constituents, whereas D is Sb and As in tetrahedrite and tennantite, respectively. Several different C constituents are known in both series, e.g., Cd, Cu, Fe, Hg, In, Mn, Ni, and Zn. This wide chemical variability, in some cases observed across an ore-field, has been used by some authors to constrain ore-forming processes (e.g., Hackbarth and Petersen, 1984; Kovalenker and Bortnikov, 1985; Staude et al., 2010; Kemkin and Kemkina, 2013; Wei et al., 2021). In common with other sulfides, TGMs are particularly prone to alteration when exposed to the oxidizing and wet conditions usually occurring close to or at the Earth surface. Owing to their content in priority pollutant metals (e.g., Sb, As, Cu, Cd, Hg; Keith and Telliard, 1979) and their widespread occurrence in several ore deposits, TGMs represent an environmental risk upon weathering conditions, being the source for several potentially toxic elements whose dispersion is influenced by the precipitation and stability of supergene

* Corresponding author at: Dipartimento di Scienze della Terra, Via S. Maria 53, 56126 Pisa, Italy.
E-mail address: massimo.dorazio@unipi.it (M. D'Orazio).

https://doi.org/10.1016/j.oregeorev.2023.105847
Received 23 August 2023; Received in revised form 20 December 2023; Accepted 20 December 2023
Available online 27 December 2023

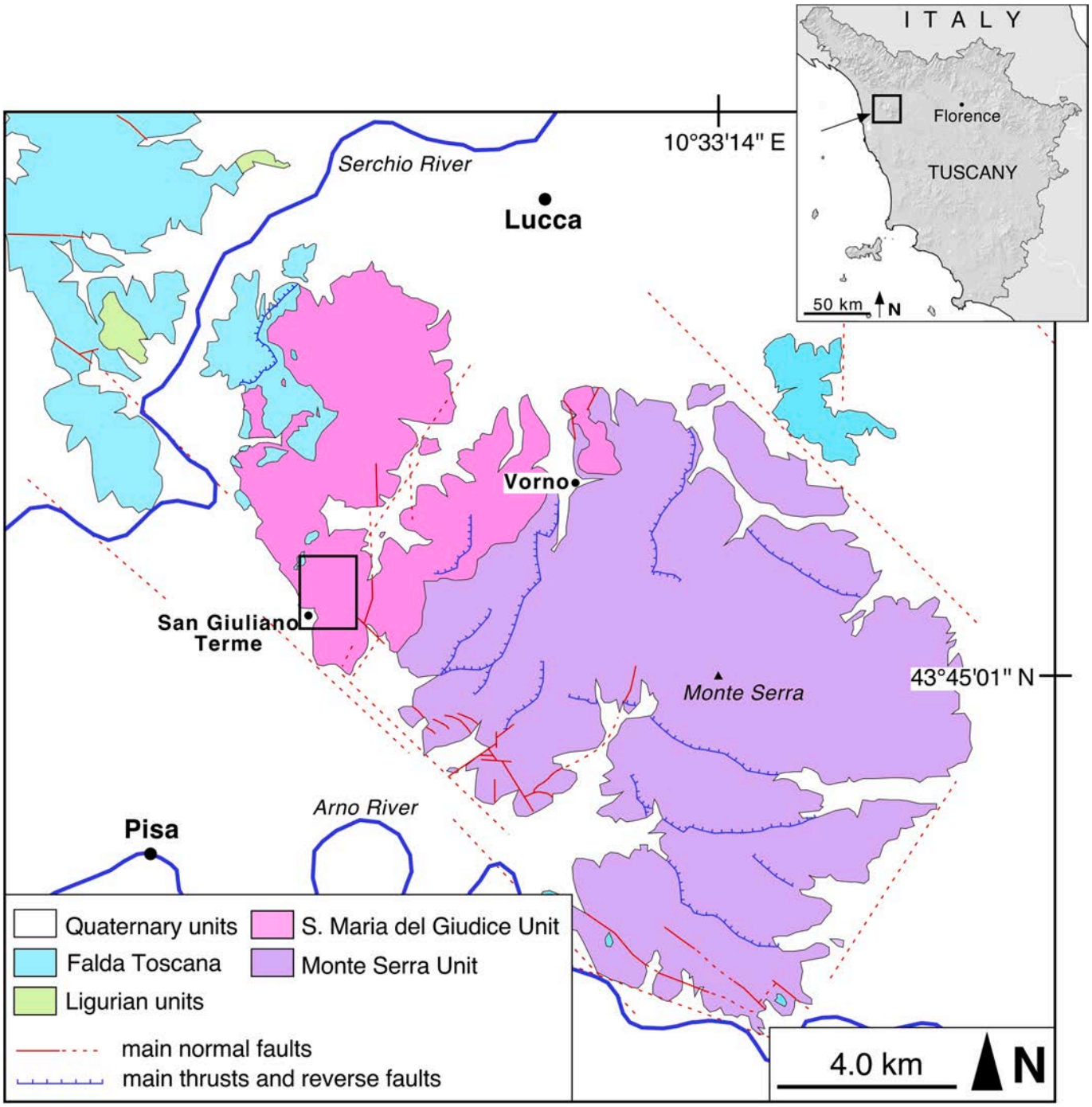

Fig. 1. Tectonic sketch map of the Monti Pisani area (Lucca and Pisa provinces, northern Tuscany). The small box encloses the area represented in Fig. 2. Redrawn and simplified after Rau and Tongiorgi (1974).

phases. Recently, some authors studied the supergene minerals derived from TGMs alteration, giving some insights about elemental mobility (e.g., Borčinová Radková et al., 2017; Keim et al., 2018; Majzlan et al., 2018). Borčinová Radková et al. (2017) and Majzlan et al. (2018) studied the alteration of a solid solution between tetrahedrite-(Fe) and tennantite-(Fe) from Špania Dolina-Piesky and Ľubietová-Svätodušná (Slovakia). Keim et al. (2018) focused their attention on Bi-bearing tennantite-(Fe/Zn) from different geological environments in the Schwarzwald ore district (Germany). It is worth noting, in agreement with Keim et al. (2018), that the alteration affecting TGMs is directly related to TGMs composition as well as to the chemistry, *p*H, and fO_2 of weathering fluids. For this reason, the results of these processes may vary in different geochemical environments and consequently observation from different geological settings can be useful.

Among the priority pollutant metals (Keith and Telliard, 1979) occurring in TGMs, one of the most common, after Sb and As, is Hg. The occurrence of this heavy element in TGMs has been known since the 19th century (see Biagioni et al., 2020b) and currently both tetrahedrite-(Hg) and tennantite-(Hg) are known (Biagioni et al., 2020b, 2021). The alteration of these Hg-bearing TGMs has not been fully described yet. Some authors (e.g., Nickel et al., 2007; Keim et al., 2018) reported the crystallization of tiny crystals of supergene cinnabar following the weathering of Hg-poor TGMs specimens. Indeed, in some cases Hg was below detection limits (e.g., Nickel et al., 2007) or lower than 0.5 wt%

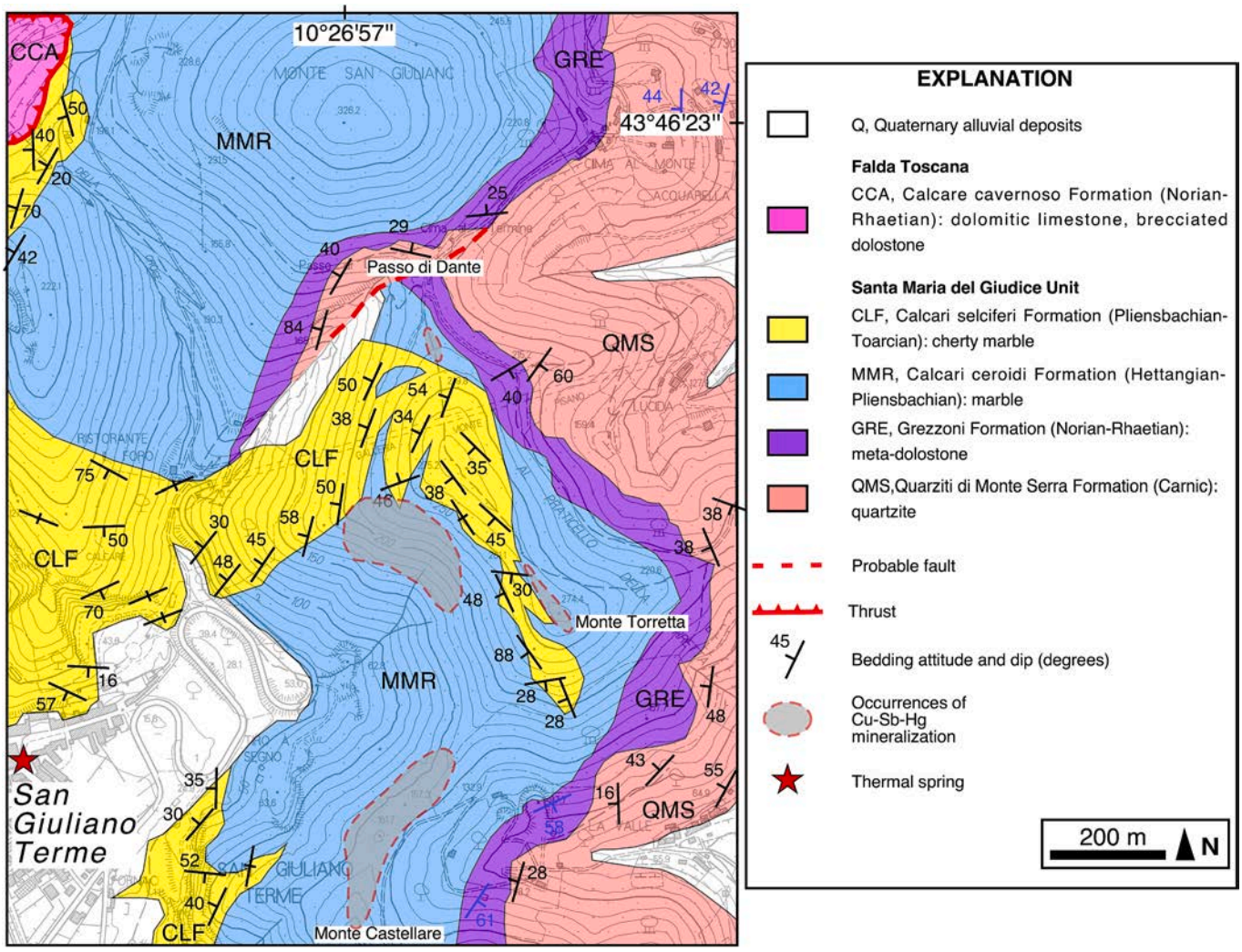

Fig. 2. Geological sketch map of the Monti Pisani area to the east of San Giuliano Terme (Pisa). Redrawn and modified from Carta Geologica della Toscana (Sezione 273020, San Giuliano Terme, 1:10.000 scale, Regione Toscana - Servizio Geologico Regionale).

(corresponding to less than 0.1 atoms per formula unit, apfu – Keim et al., 2018). On the contrary, Hg-rich TGMs produce abundant supergene cinnabar (e.g., Majzlan et al., 2019). Earthy masses of cinnabar, associated with malachite, were reported from Jurassic *meta*-carbonate rocks of the Monti Pisani metamorphic complex (Tuscany, Italy) by D'Achiardi (1873); D'Achiardi (1877), and their origin was hypothetically related to the alteration of Hg-bearing TGMs. Owing to the lack of modern data on this occurrence and aiming at describing the supergene weathering processes affecting Hg-bearing TGMs hosted in *meta*-carbonate rocks, a study of this Italian locality has been performed. In this study, the geological setting, origin, and alteration processes of this Cu-Sb-Hg mineralization located close to the San Giuliano Terme village, about 5 km north-east of Pisa, are investigated, allowing to trace the differential mobility of the chemical constituents of TGMs from hypogene to supergene environment.

2. Geological background

2.1. The Monti Pisani metamorphic complex

The Monti Pisani are a small mountain massif located in northwestern Tuscany, between the rivers Arno (to the south) and Serchio (to the north) (Fig. 1). It belongs to the Northern Apennine Chain and is part of the Middle Tuscan Ridge, a discontinuous belt of mountains and hills (from the Alpi Apuane massif to the north to the Monte Argentario to the south) where the metamorphic units of the Northern Apennines are widely exposed (e.g., Balestrieri et al., 2011).

Following Rau and Tongiorgi (1974), the current structural setting of the Monti Pisani metamorphic complex can be described as formed by two tectonic units, i.e., the Monte Serra Unit and the overlying Santa Maria del Giudice Unit. On the northwestern and southwestern borders of the massif, these metamorphic units are overlain by the non-metamorphic formations belonging to the Tuscan Nappe (Fig. 1). The Santa Maria del Giudice Unit is made of *meta*-siliciclastic rocks belonging to the "Verruca" (Anisian-Ladinian) and "Quarziti di Monte Serra" (Carnian) formations. The protoliths of these rocks were continental siliciclastic sediments that represent the beginning of the Alpine sedimentation on the continental margin of the Adria micro-plate. The *meta*-siliciclastic rocks are followed by *meta*-carbonate rocks (*meta*-dolostones, marbles, cherty marbles; Norian-Lias) and *meta*-radiolarites (Malm; Rau and Tongiorgi, 1974). Triassic-to-post-Triassic rocks of both units rest unconformably on a Paleozoic basement made of schist, phyllite, quartzite and *meta*-conglomerate. Locally, Carboniferous-Permian metapelites, known as the "Scisti di San Lorenzo" Formation, host anthracite and organic carbon-rich levels (e.g., Marini et al., 2020). The metamorphic rocks belonging to the Monte Serra and Santa Maria del Giudice units equilibrated under greenschist facies conditions during the Alpine Orogeny. The P-T conditions of the metamorphism are poorly

constrained, and range from 0.4 to 0.7 GPa and 350–400 °C, respectively (e.g., Franceschelli et al., 1986,1989,1991; Carosi et al., 1992; Leoni et al., 2009).

The structural setting of the Monti Pisani metamorphic complex mirrors that recognized in the continental tectonic units of the Northern Apennines. It developed during early compressive tectonic phases (D_1 and D_2 phases, according to Carosi et al., 1997, 2002), that were responsible for the stacking of the different tectonic units and the formation of NE-verging folds and thrusts, followed by a tectonic phase (D_3) developed in an extensional regime and related the exhumation of the deepest tectonic units. During the late-stage evolution of the Monti Pisani metamorphic complex, brittle structures, represented by faults and joints, formed (e.g., Rau and Tongiorgi, 1974; Grassi et al., 1992).

2.2. The San Giuliano Terme area

The area hosting the Cu-Sb-Hg mineralization is characterized by wide exposures of the Mesozoic *meta*-carbonate rocks of the Santa Maria del Giudice Unit, overlying quartzitic and phyllitic rocks of the "Quarziti di Monte Serra" Formation (Fig. 2). The *meta*-carbonate rocks belong to the following formations (from the bottom to the top of the stratigraphic column):

i) "Grezzoni" Formation (Norian-Rhaetian), formed by light-to-dark grey (rarely pinkish) metadolostone (Rau and Tongiorgi, 1974);

ii) "Calcari ceroidi" Formation (Hettangian-Pliensbachian): marbles and rare metadolostones, mainly composed of calcite and variable amounts of dolomite (from < 2 % to 99 %), with accessory muscovite, quartz, albite, and Fe-oxy-hydroxides (Franzini and Lezzerini, 2003);

iii) "Calcari selciferi" Formation (Pliensbachian-Toarcian): cherty marbles, mainly composed of calcite with accessory quartz, albite, K-feldspar, illite, chlorite, dolomite, and tourmaline (Franzini and Lezzerini, 1998).

The main tectonic phases, associated with ductile-style pervasive deformation, folding and metamorphism, were followed by brittle-ductile and rigid-style deformations. The transition between ductile and brittle behavior is revealed by the formation of localized extensional quartz + calcite vein systems hosted in dolomitic layers associated with marbles observed in the quarries located southwards with respect to San Giuliano Terme (Dini et al., 1998).

Brittle structures are represented by normal faults and widespread joint systems. In the San Giuliano Terme area, Grassi et al. (1992) documented two more frequent directions (N-S and NW-SE) for both the normal faults and the joints. Normal faults, usually trending N150E and N180E, are subvertical and are usually associated with thin cataclastic zones, in some cases affected by karstic features and the precipitation of spathic cave calcite deposits (Grassi et al., 1992). Joints have NS and NW-SE trending directions, inclining between 40 and 90° towards W. According to Grassi et al. (1992), normal faults are younger than the joint systems, but an age for these structures was not proposed; however, Rau and Tongiorgi (1974) reported Pliocene sediments within fractures related to normal faults.

Currently, the area of San Giuliano Terme is characterized by the occurrence of some sulfate-calcic thermal springs with temperature up to ~ 40 °C and total dissolved solids ~ 2.3 g/L, and whose circulation is probably related to the normal faults bordering the SW margin of the Monti Pisani metamorphic complex (Fig. 2; Grassi et al., 1992; Fulignati and Sbrana, 2009).

Some information about the occurrence a Cu-Sb-Hg mineralization in the San Giuliano Terme area was given by Dini et al. (1998) based on the examination of specimens kept in the mineralogical collection of the Natural History Museum of the University of Pisa and some samples provided by local mineral collectors. It is worth noting that this mineralization, although cited by D'Achiardi (1877) among the Hg ore deposits of Tuscany, has never been prospected or mined and no data about its actual tonnage and grade are currently available.

Table 1
Sampling site and description of the studied samples.

Sample	Coordinates Lat N Lon E	Description
PDD-1	43°46′09″ 10°27′04″	Black metallic grain of TGM, 7 mm in size, within red earthy material hosted in thin fractures of grey marble
PDD-2	43°46′09″ 10°27′04″	Red earthy material in thin veinlets within marble
MT-1	43°45′56″ 10°27′12″	Spathic white baryte vein within pinkish brecciated marble
MT-2	43°45′56″ 10°27′12″	Red earthy material within baryte vein. The vein is hosted in pinkish brecciated marble
MT-3	43°45′47″ 10°27′03″	Sub-millimetric grains with metallic luster within light-brown marble debris
SGT-3	43°45′44″ 10°26′59″	Marble enclosing euhedral quartz crystals

Abbreviations: TGM, tetrahedrite group mineral.

3. Materials and methods

Mineralogical, petrographic, and geochemical data were obtained on samples of ores and country rocks collected in the area shown in Fig. 2. Details on the studied samples are reported in Table 1.

3.1. Chemical analyses and micro-Raman spectroscopy

Semi-quantitative major-element analyses of the studied samples were performed using a Hand-Held XRF instrument (HH-XRF; NITON XL3t GOLDD+) at the Dipartimento di Scienze della Terra, University of Pisa.

Samples PDD-1, PDD-2, MT-2, and MT-3 were investigated with a Field Emission Gun-Scanning Electron Microscope (FEI Quanta 450 ESEM FEG) at C.I.S.U.P. Samples were mounted in epoxy resin, polished, and coated with carbon. An energy-dispersive X-ray spectrometer (Bruker QUANTAX XFlash Detector 6|10) coupled with the SEM was used to obtain chemical data on minerals and to collect X-ray maps.

Quantitative chemical analyses of selected mineral species were performed on samples PDD-1 and MT-3 using a Cameca SX100 electron microprobe (National Museum, Prague, Czech Republic) and the following analytical conditions: wavelength dispersive spectroscopy mode, accelerating voltage 25 kV, beam current 20 nA, beam size 1 μm. The following standards and X-ray lines were used to minimize line overlap: Ag (Ag*L*α), chalcopyrite (Cu*K*α, *S**K*α), pyrite (Fe*K*α), HgTe (Hg*L*α), NiAs (As*L*β), Sb_2S_3 (Sb*L*α) and ZnS (Zn*K*α). Peak counting times were 20 s for all elements and one half of the peak time for each background. Other elements with Z > 8 were found to be below the detection limits (0.02–0.10 wt%). In sample MT-3, the chemical analysis of Cu/Ag-Hg alloys was also performed using an accelerating voltage of 15 kV, to minimize the interaction between the electron beam and the surrounding native Cu hosting the small grains of Cu/Ag-Hg alloys. Matrix correction by the PAP procedure (Pouchou and Pichoir, 1985) was applied to the data.

Micro-Raman spectroscopy was used for identifying selected mineral species using a Horiba Jobin-Yvon XplorA Plus apparatus equipped with a motorized *x-y* stage and an Olympus BX41 microscope with a 50 × objective (Dipartimento di Scienze della Terra, University of Pisa). Raman spectra were excited using a 532 nm line of a solid-state laser, with different counting times. Backscattered radiation was analyzed with a 1200 gr/mm grating monochromator. The mineral identification was performed through the comparison of the collected spectra with those reported in the RRUFF database (Lafuente et al., 2015).

3.2. Fluid inclusion analyses

Samples for fluid inclusion investigation were prepared as 100–300 μm-thick double polished thin sections to observe and analyze fluid inclusions in baryte and quartz crystals. Micro-thermometric

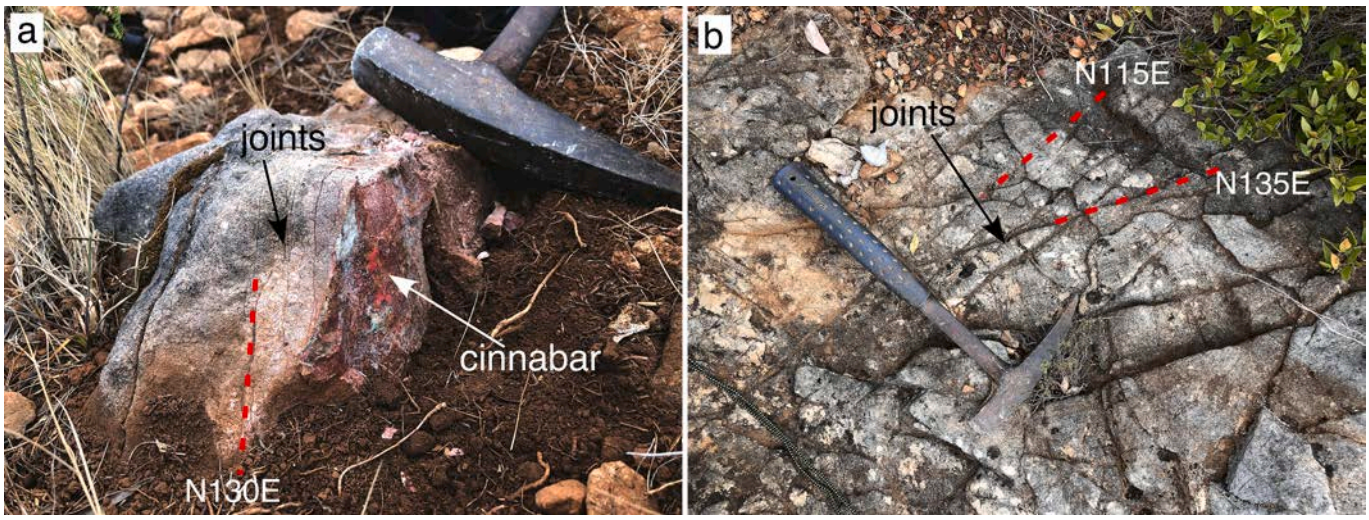

Fig. 3. Sets of joints in the Jurassic marble and marble breccia from San Giuliano Terme area. a) Set of sub-vertical joints trending N130E and hosting red cinnabar-dominated material. b) Two sets of sub-vertical joints trending N115E and N135E. (For interpretation of the references to color in this figure legend, the reader is referred to the web version of this article.)

measurements on fluid inclusions (FI) were carried out on a heating-freezing stage (Linkam THMS 600, Dipartimento di Scienze della Terra, University of Pisa), with temperature measurements accuracy of ± 2 °C at 398 °C controlled by the melting point of $K_2Cr_2O_7$, ± 0.1 °C at 0 °C and ± 0.2 °C at −56.6 °C controlled by using certified pure water and CO_2-bearing synthetic fluid inclusions (Synthetic Fluid Inclusion Reference Set, Bubbles Inc., USA). Salinity estimates of FI were determined from halite dissolution, final ice melting temperatures and

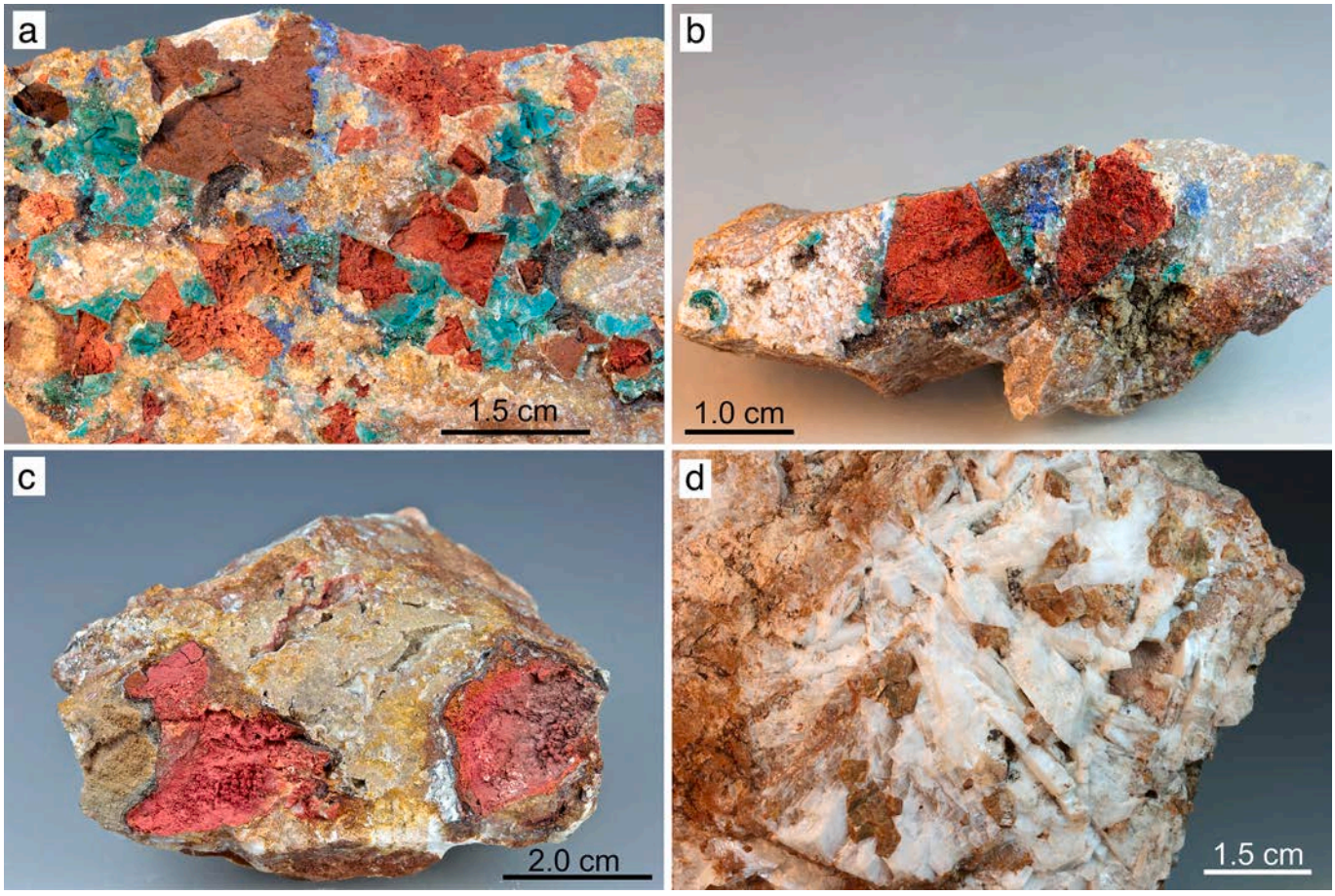

Fig. 4. Images of the main phases forming the Cu-Sb-Hg mineralization of San Giuliano Terme. a, b) Red earthy masses of cinnabar-dominated material replacing the primary tetrahedral crystals of TGM associated with malachite (green) and azurite (blue) (Passo di Dante). c) Irregularly shaped masses of cinnabar-dominated earthy material within a marble breccia (Monte Castellare). d) Baryte (white) and calcite (light brown) crystals in a sample taken from the veins cropping out close to the top of Monte Torretta. (For interpretation of the references to color in this figure legend, the reader is referred to the web version of this article.)

clathrate melting temperatures using the equations of Sterner et al. (1988) and Bodnar (1993) for the H_2O-NaCl system, and Darling (1991) for the H_2O-CO_2-NaCl system. The salinity is expressed as wt% $NaCl_{equiv.}$. Because of the low toughness of baryte, special care was taken to avoid re-equilibration of FI in baryte during heating. In particular, the heating process was conducted only once for each small baryte chip to avoid potential errors that could otherwise be caused by overheating of any individual inclusion. Moreover, in each heating run, all the inclusions of interest were monitored during this single run, with the homogenization temperatures recorded from lowest to highest. Nevertheless, several FI (particularly the two-phase vapor-rich FI, see below) decrepitated during heating runs above 200 °C. This particularly occurred for inclusions larger than about 20 μm in size.

3.3. X-ray diffraction

Single-crystal X-ray diffraction was performed on a 0.10 × 0.08 × 0.06 mm^3 grain of a TGM picked up from sample PDD-1 using a Bruker D8 Venture diffractometer operating at 50 kV and 1.4 mA and equipped with a Photon III CCD detector and monochromatized and micro-focused Mo*K*α radiation (Centro per l'Integrazione della Strumentazione Scientifica dell'Università di Pisa, C.I.S.U.P., University of Pisa). The detector-to-crystal distance was set at 38 mm. Data were collected in φ scan mode in 0.5° slices, with an exposure time of 2 s per frame, and they were corrected for Lorentz, polarization, absorption, and background effects using the package of software Apex4 (Bruker AXS Inc., 2022). The crystal structure of TGMs was refined using Shelxl-2018 (Sheldrick, 2015) starting from the atomic coordinates given by Biagioni et al., (2020b) for tetrahedrite-(Hg). The modelling of the racemic twin indicated that the structure had to be inverted. Neutral scattering factors were taken from the International Tables for Crystallography (Wilson, 1992). Details of data collection and refinement as well as fractional atomic coordinates and displacement parameters are available in the Crystallographic Information File (CIF) deposited as Supplementary Material.

X-ray powder diffraction data were collected on sample PDD-2 using a Bruker D2 Phaser diffractometer (30 kV, 10 mA), operating in Bragg-Brentano geometry (θ–θ scan mode) and equipped with a one-dimensional Linxeye detector (Dipartimento di Scienze della Terra, University of Pisa). Nickel-filtered Cu*K*α radiation was used. Data were collected in the scan range 5-65° in 2θ, with scan step of 0.02° and counting time of 0.1 s/step.

4. The Cu-Sb-Hg mineralization of San Giuliano Terme

4.1. Field occurrence

A new geological survey of the hills located immediately east and north-east of San Giuliano Terme village revealed the widespread diffusion of a Cu-Sb-Hg mineralization as thin veinlets and veins. Indeed, showings of Cu-Sb-Hg minerals may be found from Passo di Dante (43°46′14″ N 10°27′03″E) to the northwestern slope of Monte Castellare (43°45′37″ N 10°26′57″E) (Fig. 2). Mineralization is hosted within very thin planar fractures, trending N105-140E, in marble and marble breccia belonging the Early Jurassic "Calcari ceroidi" Formation (Fig. 3).

Ore minerals are represented by deeply altered TGMs, whose relicts have been very rarely found; alteration products are mainly represented by red earthy powdery materials, typically filling triangular-shaped voids, and green and blue Cu minerals (Fig. 4a, b). In other occurrences the red material forms irregular masses within very thin fractures of the marble and marble breccia without any supergene Cu mineral (Fig. 4c). Calcite, baryte, and very rare fluorite are the scarce gangue minerals. An interesting feature is represented by a set of veins of baryte, up to 4 mm in thickness, occurring close to the top of Monte Torretta, trending N135E and dipping 50° towards NE. They are hosted within a pinkish variety of variably brecciated marble and are made of centimeter-sized white bladed crystals of baryte associated with minor light-brown calcite rhombohedra (Fig. 4d). In this kind of occurrence, euhedral tetrahedral crystals of TGM fully replaced by earthy dark red supergene phases infill the spaces between the baryte crystals or are included within them.

Quartz is absent as gangue of the TGM mineralization, but idiomorphic quartz crystals occur scattered in the marble from the southern sector of the mineralized area.

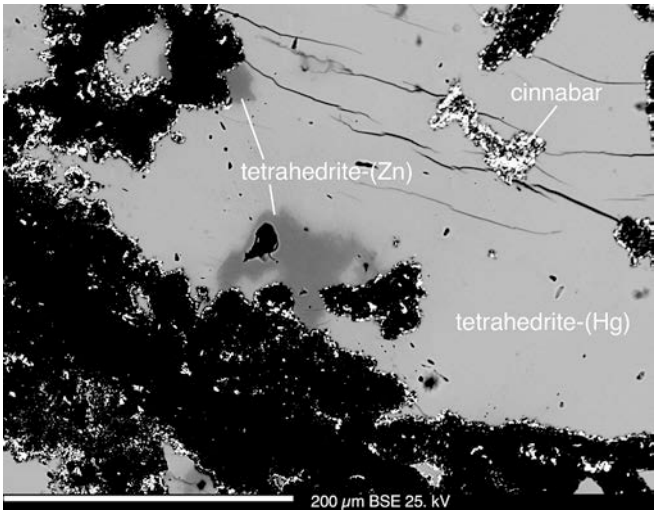

Fig. 5. Backscattered electron image showing some grains of tetrahedrite-(Hg) enclosing patchy zones of darker tetrahedrite-(Zn) from sample PDD-1. The white nanometric particles are cinnabar, whereas the black areas are made of malachite + phases of the romèite group.

Table 2
Electron microprobe data (average, range, estimated standard deviation; wt%) of TGMs from San Giuliano Terme.

	Tetrahedrite-(Hg)			Tetrahedrite-(Zn)		
Constituent		n = 51	e.s.d.		n = 12	e.s.d.
Cu	33.77	33.32 – 34.30	0.21	37.10	35.78 – 37.63	0.60
Ag	0.11	0.00 – 0.48	0.08	0.03	0.00 – 0.09	0.04
Fe	0.88	0.72 – 1.02	0.07	0.67	0.58 – 0.85	0.09
Zn	0.13	0.05 – 0.69	0.05	4.91	3.24 – 5.68	0.81
Hg	17.59	16.62 – 18.14	0.33	5.17	3.15 – 9.19	1.94
As	2.25	1.94 – 2.90	0.23	1.82	1.55 – 1.99	0.17
Sb	23.01	21.79 – 23.78	0.41	26.07	25.18 – 26.49	0.38
S	22.25	22.01 – 22.55	0.13	24.30	23.57 – 24.88	0.38
Total	99.99	99.15 – 100.78	0.40	100.07	99.72 – 100.54	0.30
Atoms per formula unit based on ΣMe = 16						
Cu	9.92	9.86 – 9.95	0.02	9.99	9.93 – 10.03	0.03
Ag	0.02	0.00 – 0.08	0.01	0.00	0.00 – 0.01	0.01
Fe	0.30	0.24 – 0.34	0.02	0.21	0.18 – 0.27	0.03
Zn	0.04	0.01 – 0.20	0.04	1.28	0.87 – 1.46	0.20
Hg	1.64	1.53 – 1.70	0.04	0.44	0.26 – 0.81	0.17
As	0.56	0.49 – 0.73	0.06	0.41	0.36 – 0.45	0.04
Sb	3.53	3.36 – 3.64	0.06	3.66	3.62 – 3.72	0.03
S	12.95	12.82 – 13.04	0.05	12.96	12.84 – 13.06	0.06
Ev(%)	0.9	0.2 – 2.0	0.4	0.6	0.1 – 1.2	0.4

Note: *n* = number of spot analyses; e.s.d. = estimated standard deviation; Ev(%) = [Σ(val +) – Σ(val–)] × 100 / Σ(val–). Iron assumed as Fe^{2+}.

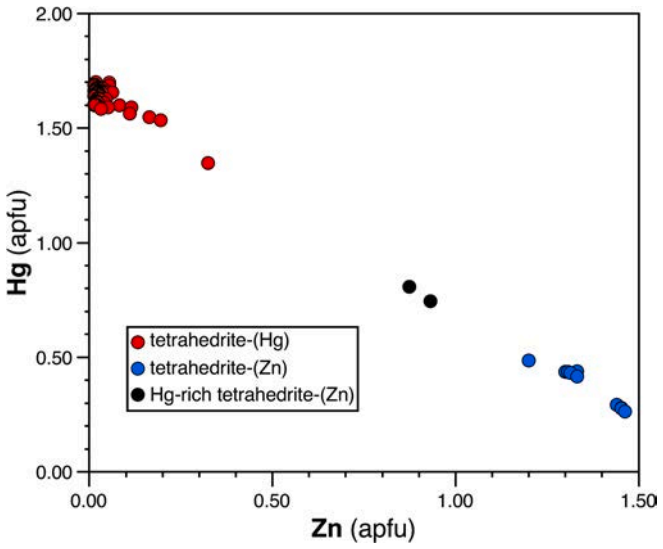

Fig. 6. Mercury vs Zn (in atoms per formula unit, apfu) for the TGMs from sample PDD-1.

4.2. Mineralogy

4.2.1. Tetrahedrite-group minerals

Unaltered tetrahedrite group minerals are very rare in the San Giuliano Terme area. Few dark grains with metallic luster were observed in samples PDD-1, MT-1, and MT-3. In the PDD-1 sample, TGMs occur as anhedral relict grains up to 7 mm in size. Back-scattered electron (BSE) images (Fig. 5) show that two different kinds of TGMs occur: the most abundant one is Hg-rich and is light grey in BSE, whereas irregular domains of dark grey TGM are Zn-rich. Table 2 gives electron microprobe analyses of both domains.

Electron microprobe analysis of Hg-rich domains corresponds to the chemical formula $Cu_{9.92}Ag_{0.02}(Hg_{1.64}Fe_{0.30}Zn_{0.04})_{\Sigma 1.98}(Sb_{3.53}As_{0.56})_{\Sigma 4.09}S_{12.95}$. Unit-cell parameters, based on single-crystal X-ray diffraction data, are $a = 10.4630(14)$ Å, $V = 1145.4(5)$ Å^3; these values can be compared with those given by Biagioni et al., (2020b) for tetrahedrite-(Hg) from the Buca della Vena mine (Italy), Jedová Hora (Czech Republic), and Rožňava (Slovak Republic). Unit-cell parameters of the sample from San Giuliano Terme are slightly contracted, owing to an As content higher than the Italian and Czech specimens [As/(As + Sb) atomic ratios of 0 and 0.015, respectively, to be compared with 0.137 of the San Giuliano Terme sample], and to a minor Hg content with respect to the Slovak tetrahedrite-(Hg), i.e., 1.64 vs 1.83 Hg atoms per formula unit. The crystal chemical investigation of the specimen from San Giuliano Terme agrees with the main features described by previous authors (e.g., Karanović et al., 2003; Foit and Hughes, 2004; Karup-Møller and Makovicky, 2003, 2004; Biagioni et al., 2020b). The three-fold coordinated *M*(2) has an average bond distance of 2.254 Å and it is fully occupied by Cu. The tetrahedrally coordinated *M*(1) site has average bond distance of 2.387 Å and its mean atomic number, 43.0 electrons per site, agrees with the occupancy $^{M(1)}(Cu_{0.67}Hg_{0.27}Fe_{0.05}Zn_{0.01})$, corresponding to a mean atomic number of 42.6 electrons. Finally, the *X*(3) site has an average bond distance of 2.416 Å and a mean atomic number of 48.8 electrons; this corresponds to $^{X(3)}(Sb_{0.88}As_{0.12})$, in agreement with chemical formula, supporting the site occupancy $^{X(3)}(Sb_{0.86}As_{0.14})$. In conclusion, the idealized structural chemical formula of tetrahedrite-(Hg) from San Giuliano Terme can be written as $^{M(2)}Cu_6{}^{M(1)}(Cu_{4.00}Hg_{1.64}Fe_{0.30}Zn_{0.06})_{\Sigma 6.00}{}^{X(3)}(Sb_{3.45}As_{0.55})_{\Sigma 4.00}S_{13}$.

Tetrahedrite-(Zn) has empirical chemical formula $Cu_{9.99}(Zn_{1.28}Hg_{0.44}Fe_{0.21})_{\Sigma 1.93}(Sb_{3.66}As_{0.41})_{\Sigma 4.07}S_{12.96}$. Its Hg content is variable, ranging between 0.26 and 0.81 atoms per formula unit; as shown in Fig. 6, the amount of Hg shows a negative correlation with Zn, in agreement with the homovalent substitution $Hg^{2+} = Zn^{2+}$. No structural data are available on these Zn-rich domains. Moreover, the two different members of the tetrahedrite group occurring at San Giuliano Terme form two distinct groups of analyses. The two analyses corresponding to the Hg-rich tetrahedrite-(Zn) (black dots in Fig. 6) could be analytical artifacts, due to the interactions of the electron beam with both tetrahedrite-(Zn) and tetrahedrite-(Hg) during the analysis. Tetrahedrite-(Zn) has been identified through SEM-EDS analysis also in sample MT-3.

During the examination of deeply altered crystals in sample MT-1, very rare relict grains, up to ~ 10 μm in size, corresponding to a simplified idealized formula close to $(Ag_{3.1}Cu_{2.9})_{\Sigma 6.0}(Cu_{4.0}Hg_{1.9}Fe_{0.1})_{\Sigma 6.0}(Sb_{3.5}As_{0.5})_{\Sigma 4.0}S_{13}$ (based on one semi-quantitative EDS analysis), were observed. They were hypothetically identified as argentotetrahedrite-(Hg), a species recently described by Wu et al. (2021).

The occurrence of different species belonging to the tetrahedrite group is in keeping with the well-known zoning of TGMs, from the scale of the ore deposit down to the grain size (e.g., Wu and Petersen, 1977; Vassileva et al., 2014; George et al., 2017). Unfortunately, the lack of well-preserved crystals of TGM does not allow a description of the textural relations between the different identified species. Only the relations between tetrahedrite-(Hg) and tetrahedrite-(Zn) can be at least partially observed (Fig. 5), but their interpretation is not straightforward. Moreover, it is not clear which geological significance should be given to the Ag-rich TGM identified as small relicts in sample MT-1. However, these three different TGM species occurring in the San

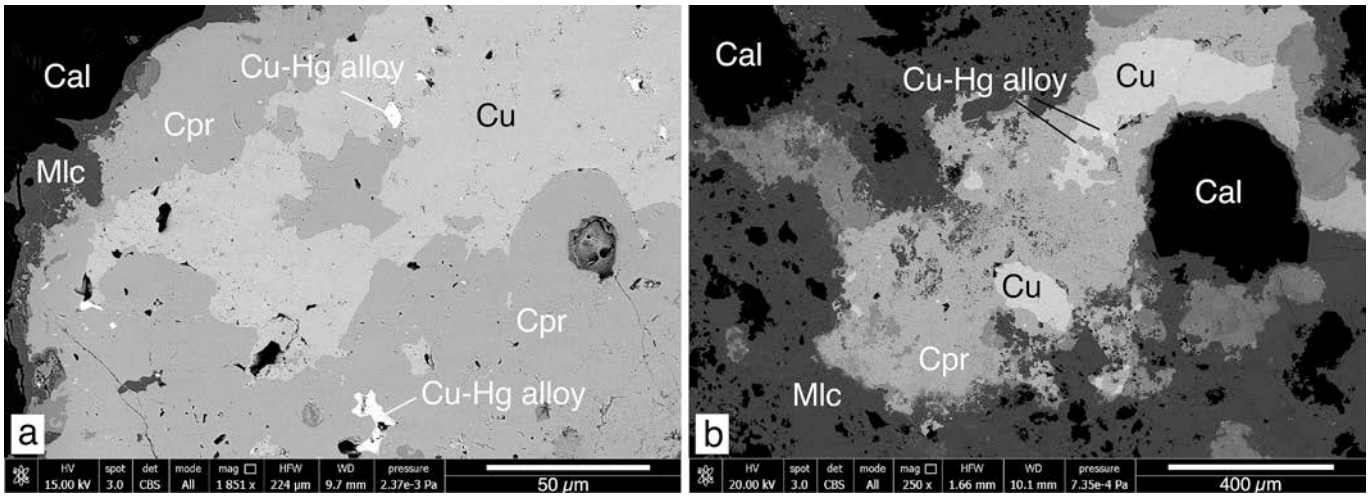

Fig. 7. Backscattered electron images of native copper grains hosting (Cu/Ag)-Hg alloys. Abbreviations (Warr, 2021): Cal, calcite, Cpr, cuprite; Mlc, malachite.

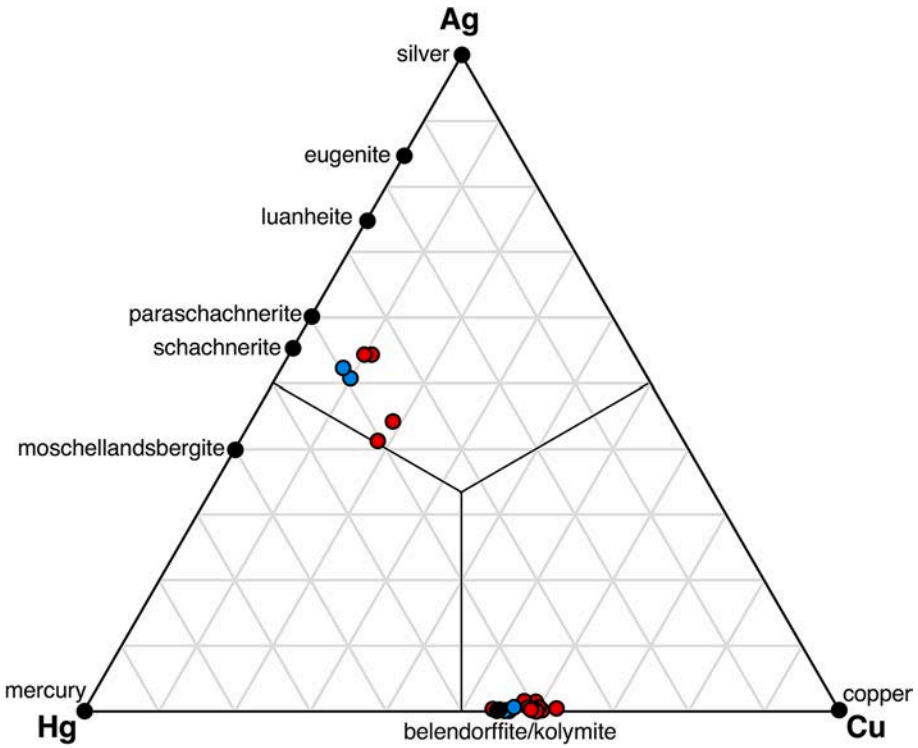

Fig. 8. Chemical composition (atoms %) of Cu-Hg and Ag-Hg alloys from San Giuliano Terme (sample MT-3). Red and light blue circles represent analytical data collected at 25 and 15 kV, respectively. Black circles indicate the chemistry of known mineral species belonging to the Ag-Cu-Hg system. (For interpretation of the references to color in this figure legend, the reader is referred to the web version of this article.)

Giuliano Terme area have some common features. All of them have an Sb/(As + Sb) atomic ratio close to 0.90, ranging from 0.82 and 0.88 for tetrahedrite-(Hg), 0.89 and 0.91 for tetrahedrite-(Zn), and, considering the quality of available data, of 0.88 for the potential argentotetrahedrite-(Hg). Moreover, they are Hg-bearing, as exemplified by the detectable content of Hg in domains corresponding to the Hg-poorest species, i.e., tetrahedrite-(Zn). Iron content was always rather low (below 0.34 apfu).

4.2.2. *Native copper and Cu/Ag-Hg alloys*

Sample MT-3 is characterized by the occurrence of anhedral grains of native copper, up to ~ 500 μm, dispersed within the light brown dolomitic marble; they are enveloped by cuprite that, in turn, is surrounded by malachite (Fig. 7a, b). Electron microprobe analyses of native copper shows only a minor content of Hg (0.41 – 0.69 wt%), without any other additional element above the detection limit.

Native copper and, more rarely, cuprite include many tiny (typically 1–10 μm and up to ~ 30 μm) rounded particles of (Cu/Ag)-Hg alloys (Fig. 7a, b). These grains are silver-grey in color, but they rapidly tarnish to black-brownish owing to an oxidation film. Electron microprobe analyses indicate the occurrence of two different phases, i.e., a Cu-Hg and an Ag-Hg alloy. Their chemical composition is plotted in Fig. 8, along with the chemistry of known mineral species in the Ag-Cu-Hg ternary system. The Cu-Hg alloy shows also minor Ag, with a (Cu + Ag)/Hg atomic ratio ranging between 1.19 and 1.68 (average 1.44); actually, owing to the small size of the analyzed grains, an excess of Cu was observed, since these alloys are hosted within native copper. Moreover, these grains are not very stable under the electron beam, in agreement with previous authors (e.g., Bernhardt and Schmetzer, 1992). For this reason, some spot analyses were performed using a lower accelerating voltage (15 kV instead of 25 kV), resulting in lower (Cu + Ag)/Hg ratios, i.e., 1.27, ranging between 1.21 and 1.34. Currently, in the Cu-Hg system the only known phases have the chemical formula Cu_7Hg_6, corresponding to a Cu/Hg ratio of 1.17. This chemistry corresponds to two dimorphs, belendorffite (Bernhardt and Schmetzer, 1992) and kolymite (Markova et al., 1980; Cipriani and Mazzetti, 1989). However, Carnasciali and Costa (2001) discussed the possible existence, within this binary system, of the compound Cu_4Hg_3 (Cu/Hg ratio of 1.33). Available data for the Cu-Hg alloy from San Giuliano Terme do not allow to solve this uncertainty. However, the presence of belendorffite and kolymite within copper and cuprite, that is in a similar occurrence as that reported in this work, is known also from Rudabánya (Hungary) (Zajzon et al., 2012).

The Ag-Hg alloy is rarer and smaller (less than 10 μm) than the Cu-Hg one and is always characterized by the occurrence of detectable Cu, probably because of the very small grain size. Indeed, whereas the grains analyzed with an accelerating voltage of 25 kV have a (Ag + Cu)/Hg atomic ratio of 1.7, this value is lowered to 1.5 using an electron beam accelerated using 15 kV. In both cases, however, the Ag/Hg ratio is close to 1.3, intermediate between the atomic ratios shown by schachnerite and paraschachnerite, i.e., 1.22 and 1.5, respectively (Seeliger and Mücke, 1972). Consequently, it is probable that the Ag-Hg alloy occurring at San Giuliano Terme could be identified as one of these two species, although Cipriani et al. (1993) questioned the actual existence of paraschachnerite.

4.2.3. *Copper sulfides*

Rims of a copper sulfide, showing a Cu/S atomic ratio (measured through EDS mode) close to 2, border the relict grains of tetrahedrite-(Hg) in sample PDD-1. The occurrence of copper sulfides as alteration products of TGMs was reported by Majzlan et al. (2018) and Keim et al. (2018). The former described the precipitation of covellite and Cu_2S-like phases (chalcocite, digenite, djurleite), whereas Keim et al. (2018) reported the presence of covellite, spionkopite, and chalcocite. The identification of these species should be based on crystallographic data; since this information is not available for sample PDD-1, this Cu sulfide will be referred hereafter as "Cu_2S-like phase".

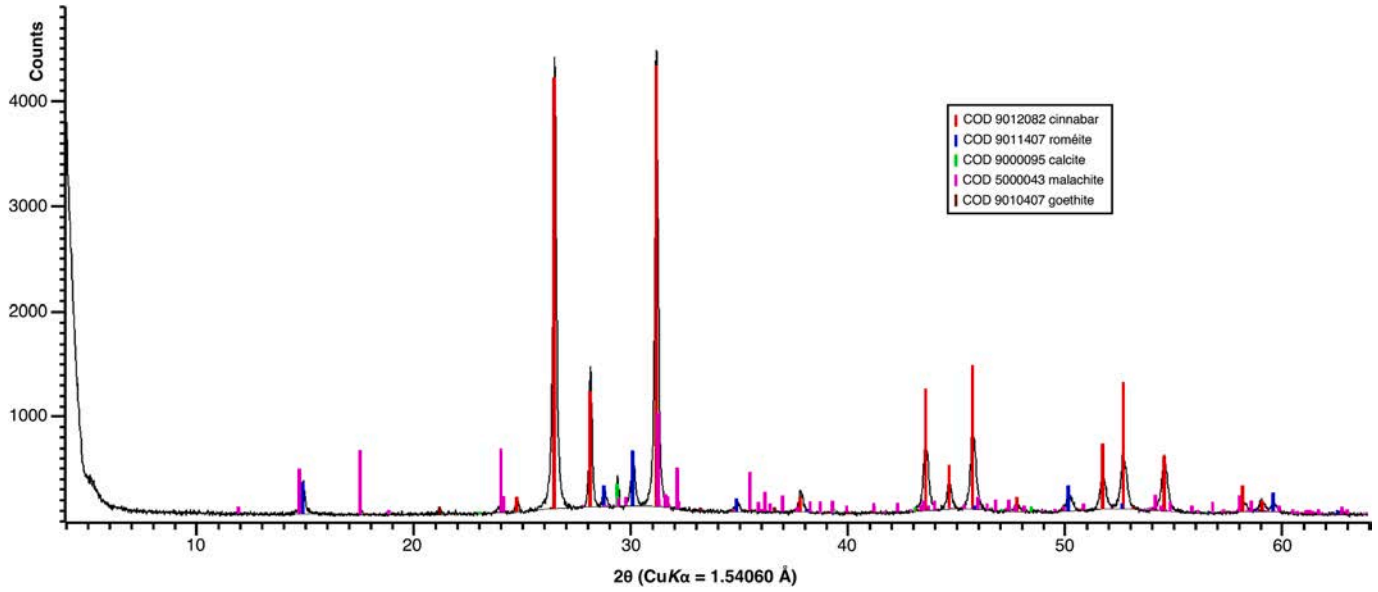

Fig. 9. X-ray powder diffraction pattern (Cu*K*α radiation) of the red earthy material in sample PDD-2. (For interpretation of the references to color in this figure legend, the reader is referred to the web version of this article.)

4.2.4. *Cinnabar*

Cinnabar has been identified as one of the main mineralogical components of the earthy red powdery material based on X-ray powder diffraction data (Fig. 9) and EDS chemical analysis, showing Hg, S, and very minor Cu as the only elements above the detection limit. Usually, cinnabar occurs as anhedral nm-to-μm size anhedral grains; less frequently, euhedral crystals have been observed included in malachite.

Cinnabar was previously reported as tiny crystals resulting from the alteration of Hg-poor specimens of TGM (e.g., Nickel et al., 2007; Keim et al., 2018), where Hg was below the detection limit or it occurred in amounts less than 0.5 wt% (corresponding to less than 0.1 atoms per formula unit, apfu). On the contrary, Hg-rich TGM produces abundant supergene cinnabar (e.g., Majzlan et al., 2019). This latter case was the same occurring at San Giuliano Terme.

4.2.5. *Oxides*

In addition to cinnabar, the alteration of TGMs gives rise to a relatively abundant mineral phase corresponding to a member of the roméite group (pyrochlore supergroup), whose identification was performed through X-ray powder diffraction (Fig. 9). This group is formed by a series of cubic oxides having general chemical formula $A_2Sb_2^{5+}O_6Y$; in currently known mineral species belonging to this group, A = Na^+, Ag^+, Ca^{2+}, Fe^{2+}, Pb^{2+}, Sb^{3+}, Bi^{3+}, and vacancy, and Y = O^{2-}, $(OH)^-$, and F^- (Atencio et al., 2010; Christy and Atencio, 2013). EDS chemical analyses showed the occurrence of Ca and Sb, with minor Fe, Si, As, and, in some cases, Na; Cu erratically occurs in the spot analyses, as well as Hg, thus suggesting that they are at least partially related to the presence of admixed phases. This statement seems to be surely applicable to Hg, where the higher contents are associated with the appearance of the *K* line of S. On the contrary, the possible occurrence of Cu in roméite-group minerals (RGM) remains questionable. The species "partzite", ideally $Cu_2Sb_2O_7$, was recently discredited by Mills et al. (2016); however, CuO contents up to 8.69 wt% have been reported by Mills et al. (2017) for hydroxyferroroméite, a species deriving from the alteration of TGMs. For this reason, the possible occurrence of minor structurally bonded Cu in RGM from San Giuliano Terme cannot be fully discarded. Silicon could be associated with amorphous silica phases or can be partially hosted in the pyrochlore-structure (Atencio et al., 2010 and references therein), whereas As has been reported from other pyrochlore-supergroup mineral occurrences. For instance, Christy and Gatedal (2005) measured up to 2.88 wt% As_2O_5 in a roméite-group mineral from Långban, Sweden, and Mills et al. (2017) gave 0.15 wt% As_2O_5 in hydroxyferroroméite. Majzlan et al. (2018) questioned the role of As^{5+} in pyrochlore-supergroup minerals, whereas Borčinová Radková et al. (2017) hypothesized the occurrence of As^{3+} as an *A*-site cation in roméite. Owing to the minor content of As in RGM from San Giuliano Terme, this does not affect its identification. The same probably holds for Fe, that could occur as Fe^{3+} (hosted at the octahedrally-coordinated *B* site) or Fe^{2+}, hosted at the *A*-site as in hydroxyferroroméite (Mills et al., 2017). Calcium, partially replaced by minor Na, and Sb are thus the main chemical constituents of the RGM in the studied samples. The lack of knowledge on the actual oxidation state of Sb as well as on the H_2O content precludes an identification at the species-level of the studied phase, i.e., hydroxycalcioroméite or oxycalcioroméite (Atencio et al., 2010; Christy and Atencio, 2013).

Other oxide phases identified in the San Giuliano Terme area are cuprite and goethite. The former has an uncertain relation with TGMs, having been identified only as an envelope around native copper in sample MT-3; cuprite was reported as an alteration product of tennantite by Borčinová Radková et al. (2017), in association with chrysocolla. Goethite was identified through X-ray powder diffraction as a very minor mineralogical constituent of the earthy red powdery material replacing TGMs; its scarcity, confirmed by its rare identification during SEM-EDS study, is possibly due to the low Fe-content of TGMs from San Giuliano Terme.

4.2.6. *Copper carbonates*

Malachite and azurite are the two Cu carbonates observed as alteration products of TGMs in the studied specimens, with the former more common than the latter, in agreement with their stability relations (e.g., Vink, 1986). Indeed, whereas malachite is widespread in all the sampled sites, being identified also as a minor mineralogical component of the earthy red powdery material replacing TGMs, azurite was abundant only in the Passo di Dante area. Malachite occurs as coatings or colloform aggregates replacing TGMs or as sprays or hemispherical aggregates, up to 5 mm in size, of green acicular crystals in small vugs within marble; azurite, whose identification was confirmed through micro-Raman spectroscopy, was observed as coatings or rare aggregates of tabular prismatic crystals, dark blue in color, up to 3 mm in length.

4.2.7. *Other mineral species*

Calcite is the main gangue mineral hosting TGMs; EDS chemical

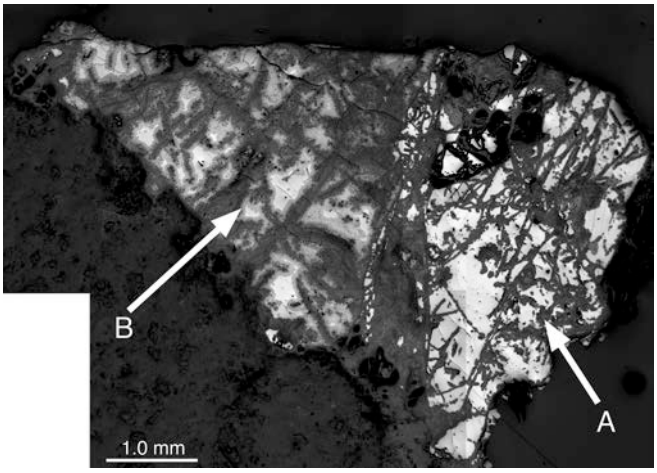

Fig. 10. Plane-polarized reflected light mosaic image (greyscale) of the partially preserved TGM relict from Passo di Dante (sample PDD-1). The two arrows point to the portions (A and B) characterized by different alteration patterns (A: stage 1 alteration; B: stage 2 alteration).

analysis shows Ca as the only element with $Z > 9$. Magnesium and Fe are below the detection limit; scalenohedral colorless crystals have been observed in small vugs.

Sample MT-2 was unusual, being characterized by a baryte vein. Semi-quantitative EDS chemical analysis points to the composition $(Ba_{0.92}Sr_{0.07})_{\Sigma 0.99}SO_4$. Baryte forms white spathic aggregates and very rarely some tabular crystals were observed. Anhedral grains of baryte, less than 10 μm in size, were also identified in the earthy red powdery material deriving from the alteration of TGMs. EDS chemical data of this latter material showed only Ba and S as elements with $Z > 9$ above the detection limit. The presence of baryte as a supergene phase in the alteration products of TGMs was reported by Majzlan et al. (2018).

Finally, fluorite was identified in only one sample from the Monte Torretta slope, as colorless vitreous crystals, with a perfect {1 1 1} cleavage, up to 2 mm in size, associated with calcite and deeply altered TGM. Its identification was supported by micro-Raman spectroscopy.

Euhedral, colorless, prismatic quartz crystals, up to 2.5 mm in length, have been frequently observed within the marble from the southern sector of the mineralized area; however, we did not find any evident relationship between the growth of this mineral and the TGM mineralization.

4.3. Supergene weathering stages of TGMs

The three samples (PDD-1, PDD-2, MT-2) studied in detail through

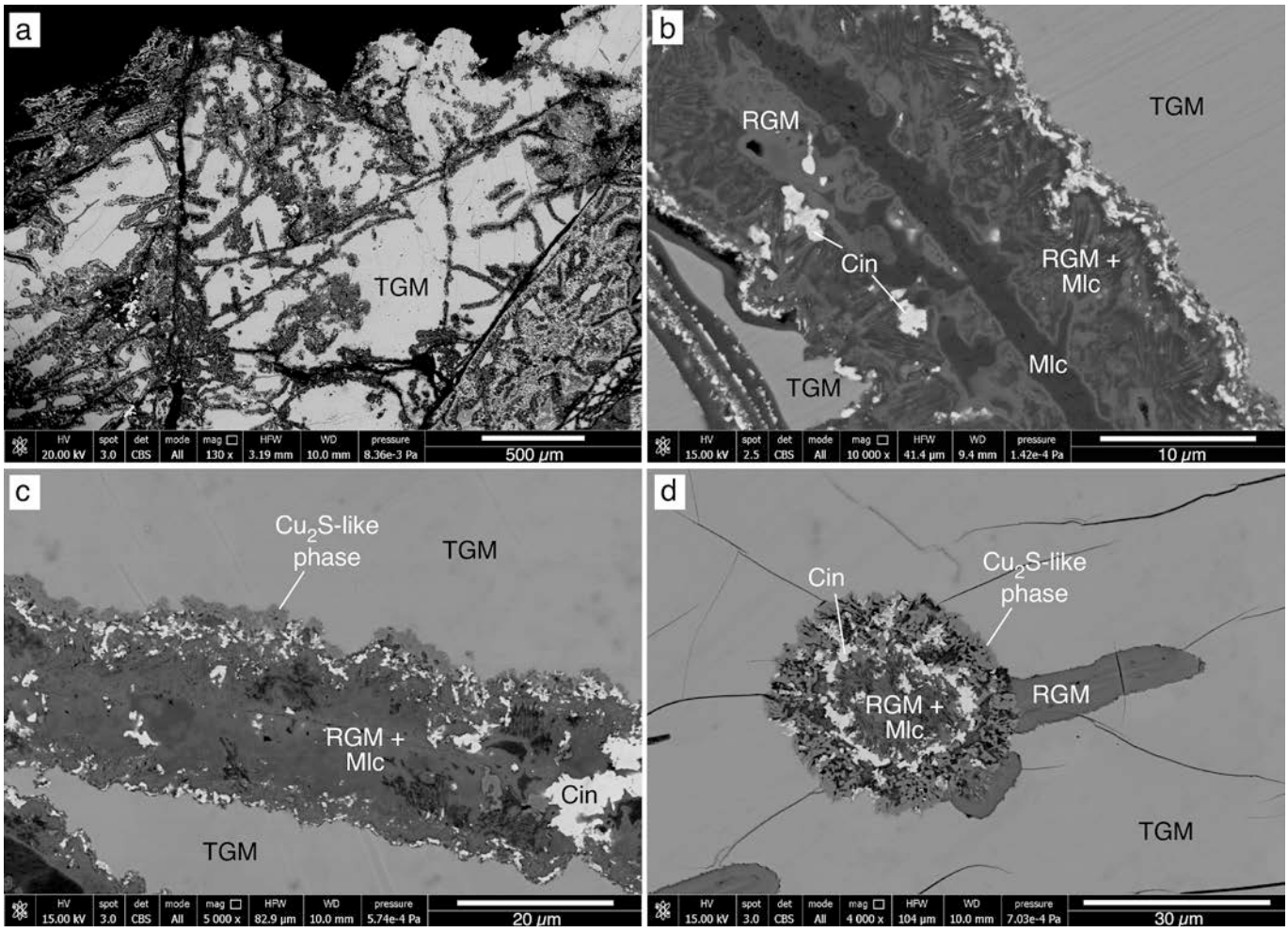

Fig. 11. Backscattered electron images of portion A (stage 1 alteration) of sample PDD-1. a) General view of portion A of Fig. 10 showing the finger-like tubes of alteration minerals pervading the unaltered TGM relict. b, c) Close-up of finger-like tubes. d) Cross-section of a finger-like tube. Note that the Cu_2S-like phase, when present, is in direct contact with the TGM. Abbreviations (after Warr, 2021): Cin, cinnabar, Mlc, malachite; RGM, Roméite Group Mineral; TGM, Tetrahedrite Group Mineral.

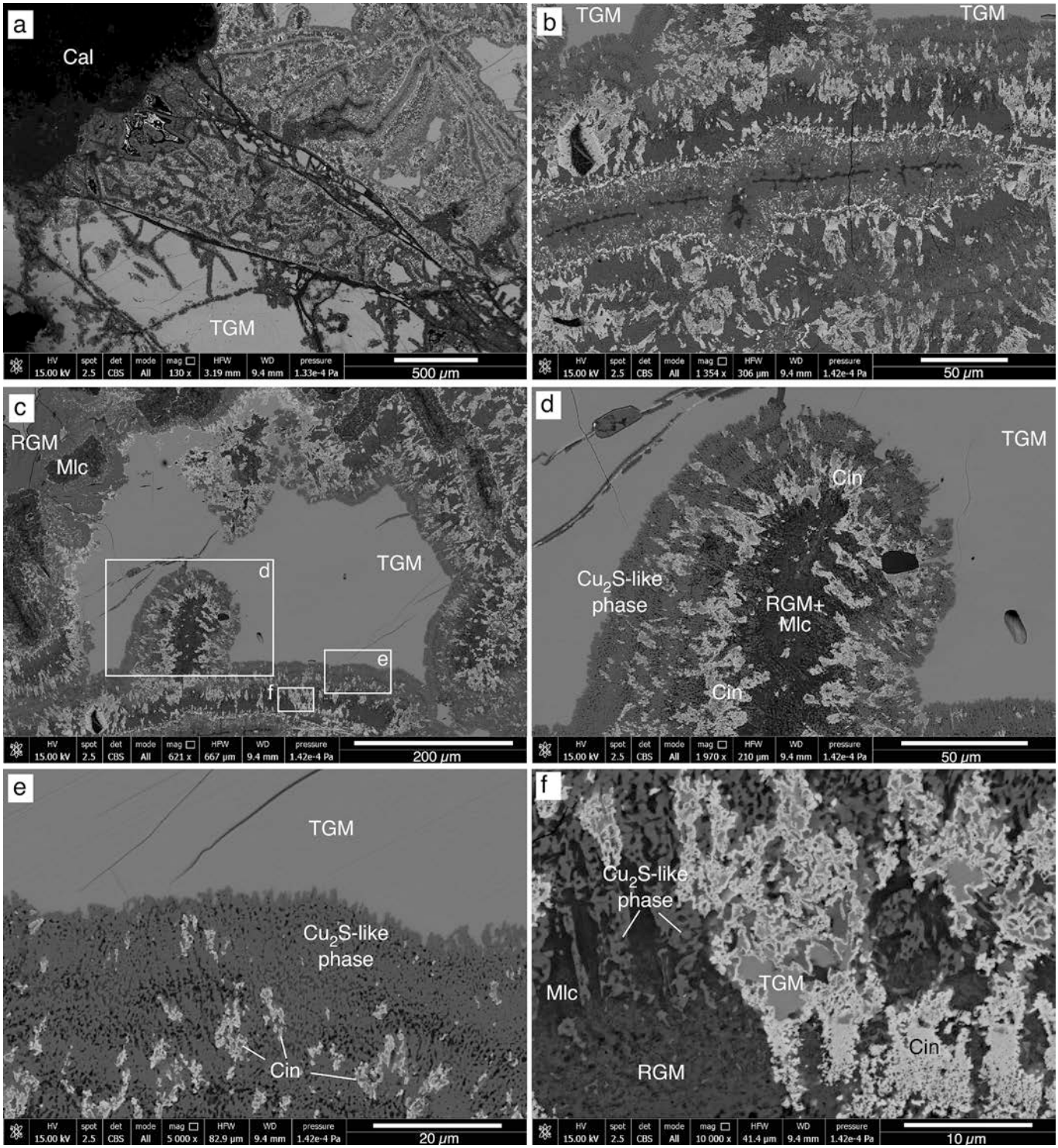

Fig. 12. Backscattered electron images of portion B (stage 2 alteration) of sample PDD-1. a) General view of portion B of Fig. 10 showing the contact with portion A. b) Finger-like tube of fine-grained alteration minerals embedded into a material made of the same minerals but with a larger grain size and in contact with relict TGM (uppermost side of the picture). c) Relict of TGM surrounded by multiple layers of alteration minerals. d) Close-up view of (c) showing the details of the layers. e) Close-up view of (c) showing the layers of Cu_2S-like phase in direct contact with the relict of TGM. Immediately away from the contact the Cu_2S-like phase is intergrown with subordinate amounts of cinnabar and malachite. f) Close-up view of (c) showing details of the layer further away from the contact with the TGM relict. Abbreviations (after Warr, 2021): Cal, calcite; Cin, cinnabar, Mlc, malachite; RGM, Roméite Group Mineral; TGM, Tetrahedrite Group Mineral.

optical and scanning electron microscopy allowed us to document the supergene alteration stages of TGMs; moreover, HH-XRF spectra were collected on these three samples. Alteration stages have been defined based on textures, mineral assemblages, and relative abundances of the different minerals.

The first two stages of alteration are both represented in sample PDD-1 which contains a relatively large mass (maximum width ≈ 7 mm) of partially altered TGM. Indeed, this mass is divided into two portions (A and B) characterized by different alteration patterns and alteration intensity (Fig. 10). Sample MT-2 contains well-formed tetrahedra of

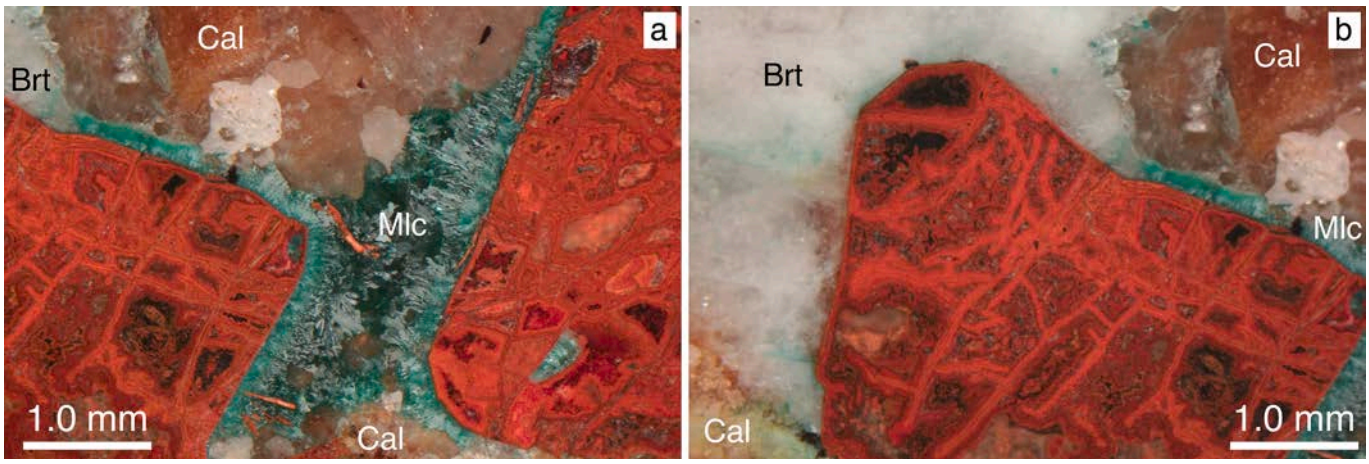

Fig. 13. Reflected light (crossed polars) images of the red earthy material filling the tetrahedral voids found within the marble-hosted baryte veins of Monte Torretta (sample MT-2). a) Two masses showing cellular texture in contact with baryte (white), calcite (light brown) and acicular crystals of malachite (green). b) A mass showing cellular texture enclosed in baryte and partially covered by malachite. Abbreviations (Warr, 2021): Brt, baryte; Cal, calcite; Mlc, malachite. (For interpretation of the references to color in this figure legend, the reader is referred to the web version of this article.)

former TGM almost completely replaced by alteration products and represents the third stage of alteration. Sample PDD-2 is a shapeless mass of red earthy powdery material representing the final and most widespread alteration stage.

4.3.1. Stage 1

The portion A of sample PDD-1 is characterized by wide areas (~40 vol%; Fig. 10) of unaltered TGM (the primary ore) pervaded by an irregular network of tiny finger-like tubes, from 10 to 50 μm wide, made of alteration products (Fig. 11b). The finger-like tubes neither show any preferred orientation nor seem to propagate from pre-existing microfractures. Typically, they terminate in sub-spherical shape. The internal structure of the tubes is quite complex and can vary mostly as a function of their thickness. The most common structure is made of a very thin layer of pure Cu_2S-like phase in direct contact with the pristine TGM, followed by a layer made of cinnabar, Cu_2S-like phase, and malachite (Fig. 11b, c, d). The most internal and volumetrically abundant part of the tubes is made of RGM along with malachite and cinnabar. In some cases, RGM occur with two different textures: 1) lamellar crystals intergrown with malachite; 2) colloform masses enveloping relatively large malachite masses (Fig. 11b). Texture 1 is generally more external than texture 2. Malachite may also form long threads at the core of the tubes (Fig. 11b).

4.3.2. Stage 2

The portion B of sample PDD-1 has much less abundant TGM relicts (~9 vol%; Fig. 10) and hence could represent a more advanced stage of alteration with respect to stage 1. The finger-like tubes are still visible, but they are thicker and surrounded by alteration minerals with a larger grain size (Fig. 12a, b).

A typical texture is that shown in Fig. 12b. Here, a finger-like tube is separated from the TGM relict by a complex-textured material made of minerals arranged in the following way: at the contact with the larger TGM relict several layers of Cu_2S-like phase with variable porosity occur. They are associated to increasing (away from the TGM) amounts of cinnabar, malachite and small TGM relicts (Figg. 12b, c, d, e, f). These layers are followed by domains made of prevailing RGM along with minor amounts of cinnabar and malachite (Fig. 12b, c, d, f).

4.3.3. Stage 3

The red earthy material filling the tetrahedral voids found within the baryte veins of Monte Torretta (sample MT-2) is representative of stage 3 alteration. This latter is characterized by a cellular texture with individual "cells" from about 0.1 to 1 mm in size (Fig. 13a, b; Fig. 14a, b, c). The relicts of TGM are extremely rare and confined to the most internal part of the "cells" (Fig. 14c), whereas the Cu_2S-like phase is completely lacking. The mineral phases forming the red earthy material are cinnabar, malachite and RGM. They are generally organized in parallel bands where the relative proportions of the three minerals and their grain size may vary to a great extent (Fig. 14b, c, d, e). The "cells" may also be occupied by voids (Fig. 14a), by larger malachite masses hosting euhedral crystal of cinnabar up to 10 μm in size (Fig. 14d), or by larger masses of RGM (Fig. 14f).

4.3.4. Stage 4

The red earthy powdery material of sample PDD-2 represents the stage 4 alteration. In this sample, cinnabar, malachite, and RGM are intermixed forming irregularly shaped masses. Cinnabar is largely prevailing (Fig. 15a, b; Fig. 16a, d) and forms nano-crystals arranged into multiple concentric layers separated by voids and/or subordinate RGM and malachite (Fig. 15a, b; Fig. 16a, b, c). The X-ray maps show that the red earthy material of this sample is relatively enriched in Fe with respect to the other samples (Fig. 16e).

4.3.5. Chemical changes in the different weathering stages

A qualitative comparison between the abundance of Hg, Cu, and Sb in the different weathering stages can be obtained comparing the HH-XRF spectra collected on samples PDD-1, MT-2, and PDD-2 (Fig. 17). A progressive increase in the ratios Hg/Sb, Hg/Cu, and Sb/Cu as the alteration proceeds is evident, in keeping with the observed modal mineralogy of the alteration products of TGMs from the San Giuliano Terme area.

4.4. Petrography and micro-thermometry of fluid inclusions

Fluid inclusions (FI) were found and studied in quartz crystals embedded in the marble (sample SGT-3) and in baryte crystals from the veins crosscutting the brecciated marbles of Monte Torretta (sample MT-1; Fig. 4d). All descriptions refer to fluid-inclusion assemblages (FIA), as defined by Goldstein and Reynolds, (1994). A FIA defines a group of fluid inclusions entrapped by the most finely discriminated events through petrographic means (Goldstein, 2003; Chi et al., 2021). The inclusions observed were assigned a probable primary or secondary origin according to the criteria of Roedder (1984) and Goldstein (2003) and were classified according to phase types observed at room temperature.

Quartz crystals embedded in marble contain multiphase (liquid + vapor + daughter mineral) liquid-rich FI (Type 1; LVHS). Type 1 FI are

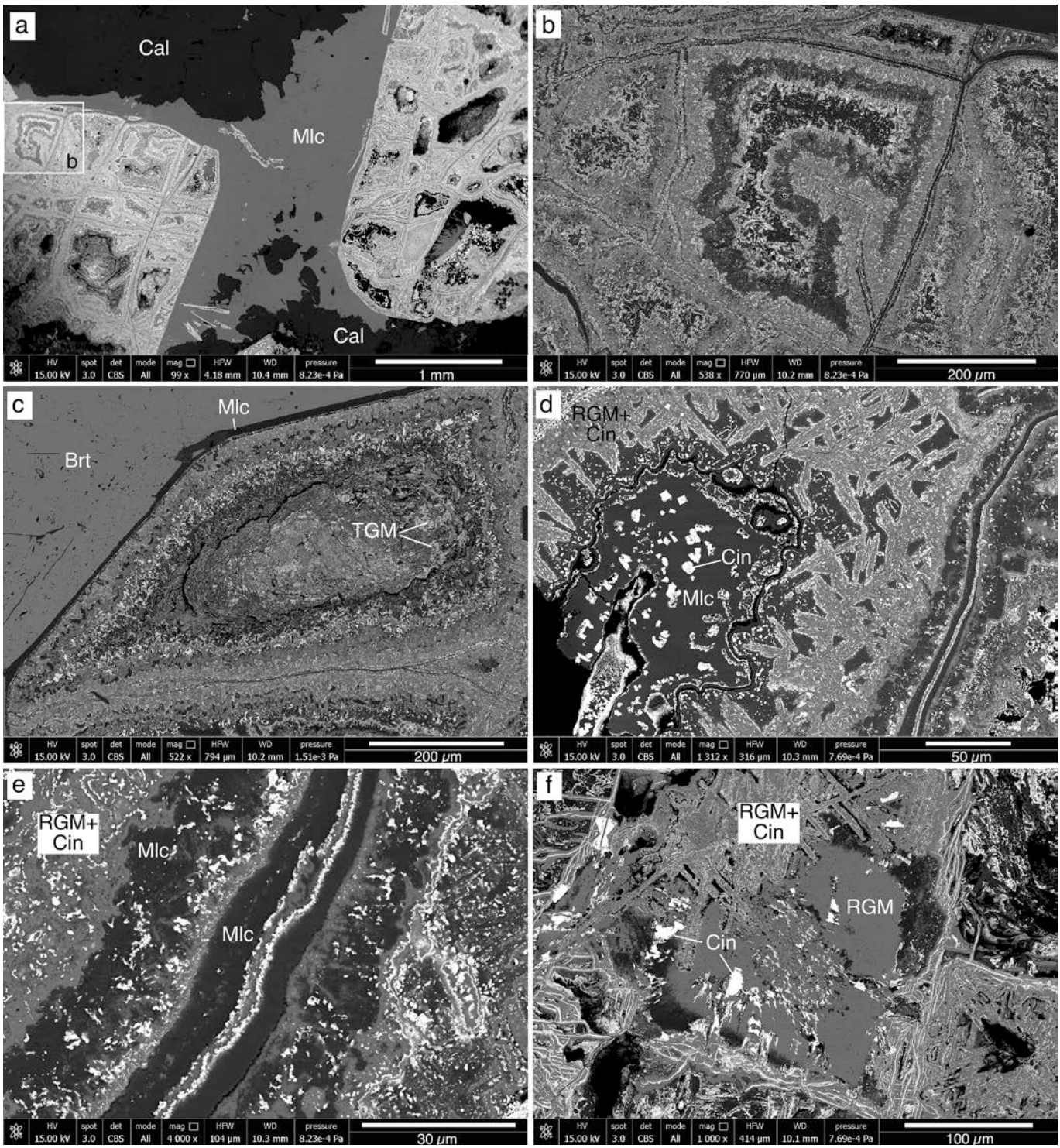

Fig. 14. Backscattered electron images of sample MT-2 (stage 3 alteration). a) Two triangular-shaped masses of red earthy material (light grey) in contact with the marble country rock (calcite, dark grey) and malachite (medium grey) and showing a cellular texture. Note the tuft of acicular crystals of malachite grown into a void of the triangle on the right side. b) Close-up of (a) showing the complex banded texture of the alteration minerals within a "cell". c) Detailed view of a banded "cell" close to the contact with the baryte gangue and containing small TGM relicts at its core. d) Detailed view of a "cell" showing blades of RGM decorated by nano-crystals of cinnabar and a core filled by malachite enclosing micrometer-sized euhedral cinnabar crystals. e) Detailed view of a zone separating two "cells" showing the banded arrangement of cinnabar (light grey), RGM (medium grey) and malachite (dark grey) and the variable grain size of these minerals. f) Relatively large domain of RGM enclosing micro-crystals of cinnabar. Abbreviations (after Warr, 2021): Cal, calcite; Cin, cinnabar, Mlc, malachite; RGM, Roméite Group Mineral; TGM, Tetrahedrite Group Mineral.

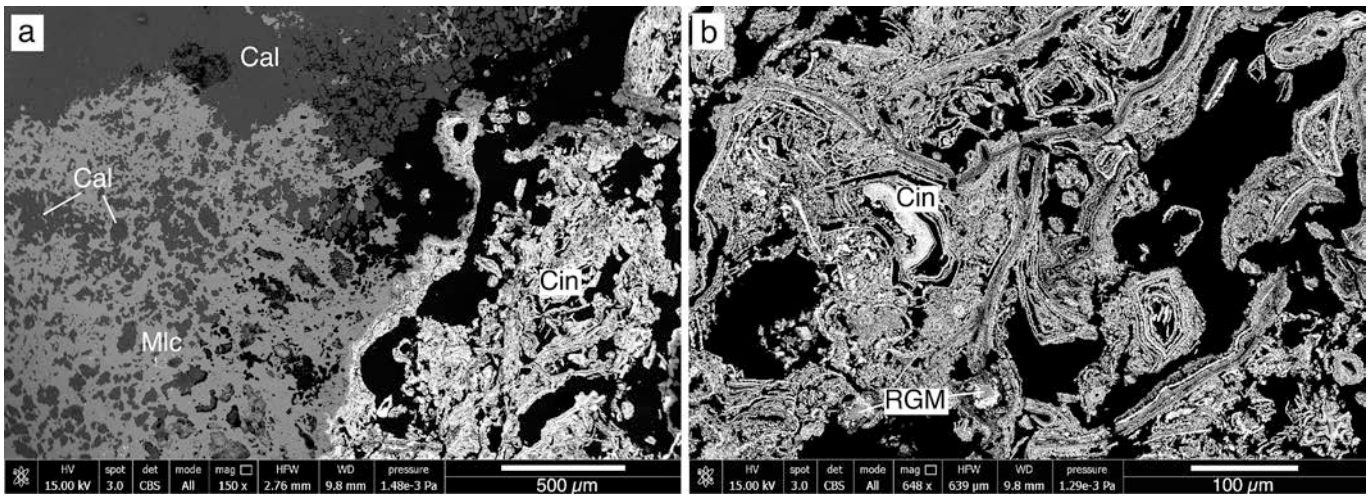

Fig. 15. Backscattered electron images of sample PDD-2 (stage 4 alteration). a) Mass of red earthy powdery material (light grey) in contact with the marble country rock (calcite, dark grey) and malachite (medium grey). Note the relicts of calcite within malachite. b) Detail of the red earthy powdery material dominated by cinnabar nano-crystals (light grey) forming multiple concentric layers. Black areas are voids. Abbreviations (after Warr, 2021): Cal, calcite; Cin, cinnabar, Mlc, malachite; RGM, Roméite Group Mineral.

between 10 and 20 μm in size. They have often ellipsoidal morphologies, but in some cases also display an irregular shape (Fig. 18a,b). Only one daughter mineral was observed within these inclusions. It is transparent, with a cubic habit, and it can be identified as halite (Fig. 18a). Type 1 FI generally form isolated clusters within the quartz crystals (Fig. 18a), thus displaying primary features (Goldstein, 2003). In some cases, FI align along trails that do not cut across all the growth zones of the host quartz crystals. This suggests a pseudosecondary origin (Fig. 18b).

Baryte crystals contain two-phase (Type 2) liquid-rich FI (LV), rare two-phase (Type 3) vapor-rich FI (VL) and monophase (Type 4) liquid only FI (L). Type 2 LV-FI are generally small (most of them are < 20 μm) and can be further distinguished in two sub-populations based on petrographic observation and micro-thermometric data: Type 2a and Type 2b. Type 2a inclusions generally occur as small clusters, suggesting a primary origin (Fig. 18c), and show a variable shape, from rounded to irregular. Type 2b and Type 3 FI often occur associated along trails that cut across the host crystals, suggesting a secondary origin (Fig. 18d,e). As reported for Type 2a FI, Type 2b and Type 3 FI show a variable morphology, from nearly rounded to irregular, and in some cases also show a platy form (Fig. 18e). Type 4 monophase L-FI always occur along trails that cut across the host crystals bearing an unambiguous secondary origin (Fig. 18f). Due to the small size of the inclusions, the petrographic relationships between the two populations of secondary FI (Type 2b/Type 3 and Type 4) are not clear. Therefore, an unequivocal interpretation of the timing of entrapment only based on microscopic observations at room temperature cannot be proposed. However, the Type 4 monophase L-FI could be considered as postdating Type 2b/Type 3 FI populations.

Micro-thermometric results of FI in quartz and baryte crystals are summarized in Fig. 19. All FI freeze to ice upon cooling below − 45/−55 °C, as clearly observed by the sudden shrinkage of the vapor bubble. Upon warming, the temperature of initial melting of ice (eutectic temperature T_e) was observed in all type of inclusions and resulted to be between − 42 °C and − 50 °C for all types of FI. These low T_e values suggest the occurrence of high concentrations of divalent cations (i.e., Ca^{2+}, Mg^{2+}) in addition to Na^+ and K^+ (Crawford, 1981) in the trapped fluids. In Type 2b and Type 3 FI, found in baryte veins, clathrate formation was observed during freezing runs. The temperature of melting of the solidified CO_2 (dry ice) was observed in some inclusions and was around –57.0 °C/−57.5 °C. This suggests the occurrence of almost pure CO_2 (triple point of pure CO_2 at − 56.6 °C).

Upon heating, Type 1 multiphase FI in quartz homogenize either by vapor bubble disappearance or by halite dissolution. The vapor bubble homogenizes (T_{hom}) in the liquid phase between 216 °C and 287 °C with a mode at 255 °C. The dissolution of halite (T_s) occurs between 207 °C and 297 °C with a mode around 285 °C, corresponding to salinity ranging between 32 and 38 wt% $NaCl_{equiv.}$, with a mode at 37 wt% $NaCl_{equiv.}$.

After freezing, during subsequent warming, Type 2a FI (LV) show a temperature of final ice melting (T_{mi}) between − 9.0 °C and − 18.2 °C with a mode around − 13.0 °C. This corresponds to salinities ranging from 12.8 and 21.1 wt% $NaCl_{equiv.}$, with a mode at about 17.5 wt% $NaCl_{equiv.}$. Upon heating, the T_{hom} varies from 247 °C to 321 °C, with a modal value at 285 °C.

In Type 2b FIs (LV) clathrate dissociation occurs (T_{cd}) between 7.5 °C and 9.0 °C with a modal value at 8.5 °C, corresponding to salinities ranging between 4.9 and 2.0 wt% $NaCl_{equiv.}$, mode around 2.5 wt% $NaCl_{equiv.}$. Few T_{hom} data were obtained on Type 2b FI, because most of them (as well as Type 3 FIs) decrepitated when heated above ~ 200 °C. The T_{hom} occurs in the range 222–242 °C.

Type 3 FI (VL) have temperatures of clathrate melting between 9.3 and 9.6 °C, corresponding to salinities between 1.4 and 0.8 wt% $NaCl_{equiv.}$. The T_{hom} in Type 3 FIs shows a range between 242 °C and 249 °C.

The T_{mi} in Type 4 FI (L) ranges from − 0.7 to 2.1 °C, corresponding to salinities ranging between 1.2 and 3.5 wt% $NaCl_{equiv.}$, with a mode around 1.5 wt% $NaCl_{equiv.}$.

5. Discussion

5.1. Genesis of tetrahedrite-(Hg) from San Giuliano Terme and its geological significance

Field evidence suggest that the formation of tetrahedrite-(Hg) at San Giuliano Terme is related to the occurrence of systems of joints and faults, indicating that these brittle structures favoured the circulation of hydrothermal fluids during the late-stage evolution of the Monti Pisani metamorphic complex. Petrographic and micro-thermometric data obtained from the different types of fluid inclusions provide a basis for the physicochemical characterization of the fluids circulating from the early to the latest stage of the hydrothermal evolution. Four populations of fluid inclusions have been identified, providing evidence for a multi-stage fluid circulation and entrapment. Three of the fluid inclusions populations (Type 2a, Type 2b-3 and Type 4) have been trapped in the

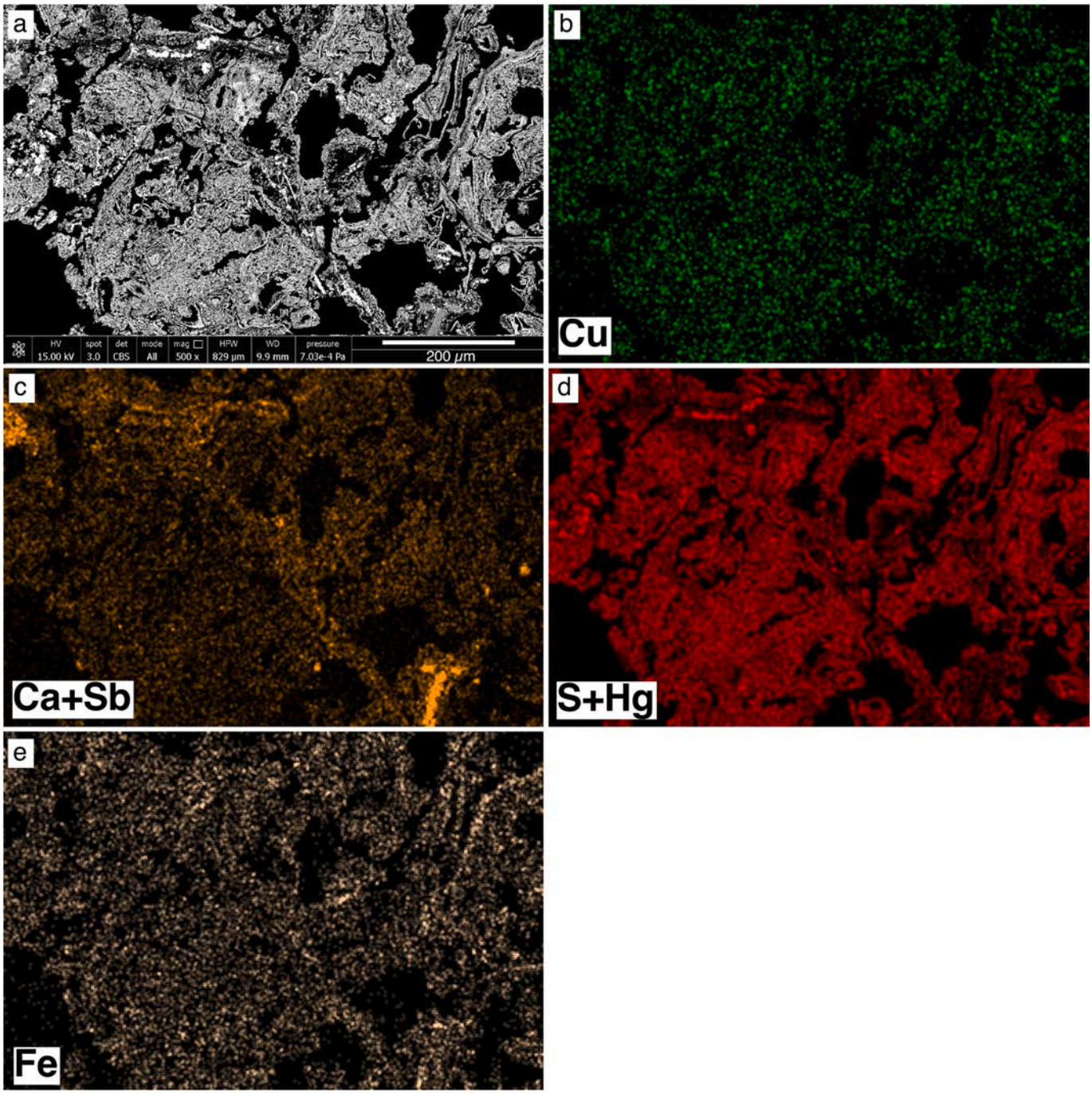

Fig. 16. X-ray maps of sample PDD-2. a) Backscattered electron image of the investigated area. b) Cu*K*α radiation. c) Ca*K*α + Sb*L*α radiation. d) S*K*α + Hg*M*αβ radiation. e) Fe*K*α radiation.

baryte gangue of the TGM mineralization. The brittle nature of the rock deformation style suggests a shallow emplacement depth for the Cu-Sb-Hg mineralization, which could be assimilated to an epithermal environment. Thus, pressure correction to the homogenization temperatures of fluid inclusions is limited and T_{hom} can be considered close to the real trapping temperature.

For this reason, the salinity and T_{hom} of the primary FI (Type 2a, LV) in baryte are believed to be representative of the fluids responsible for the Cu-Sb-Hg mineralization dominated by TGMs and are interpreted to be close to the physicochemical conditions during the mineralizing event. The hydrothermal solution was characterized by a moderately high salinity (around 17.5 wt% $NaCl_{equiv.}$) and a minimum temperature of 285 °C. In such a saline fluid, Hg could be transported as Hg-Cl complexes (e.g., Varekamp and Buseck, 1984). The association of Type 2b (LV) and Type 3 (VL) FI is suggestive of a later hydrothermal event, characterized by a low salinity (around 2.5 wt% $NaCl_{equiv.}$) fluid, which records boiling conditions at around 235–240 °C and pressure of about 3–4 MPa, thus indicating a very shallow environment. The low salinity of these FI may be taken as evidence of the massive ingression of meteoric water in the system, postdating the TGM mineralization. The latest generation of FI (Type 4) is monophase and liquid rich. These FI represent low T fluids (T < 100 °C) characterized by a still lower salinity, compared to the previous fluid circulation events (~1.5 wt% $NaCl_{equiv.}$). These fluids are similar to those presently emerging in the San Giuliano Terme thermal springs (Fulignati and Sbrana, 2009). This last fluid inclusion assemblage may be taken as evidence that cold and low salinity

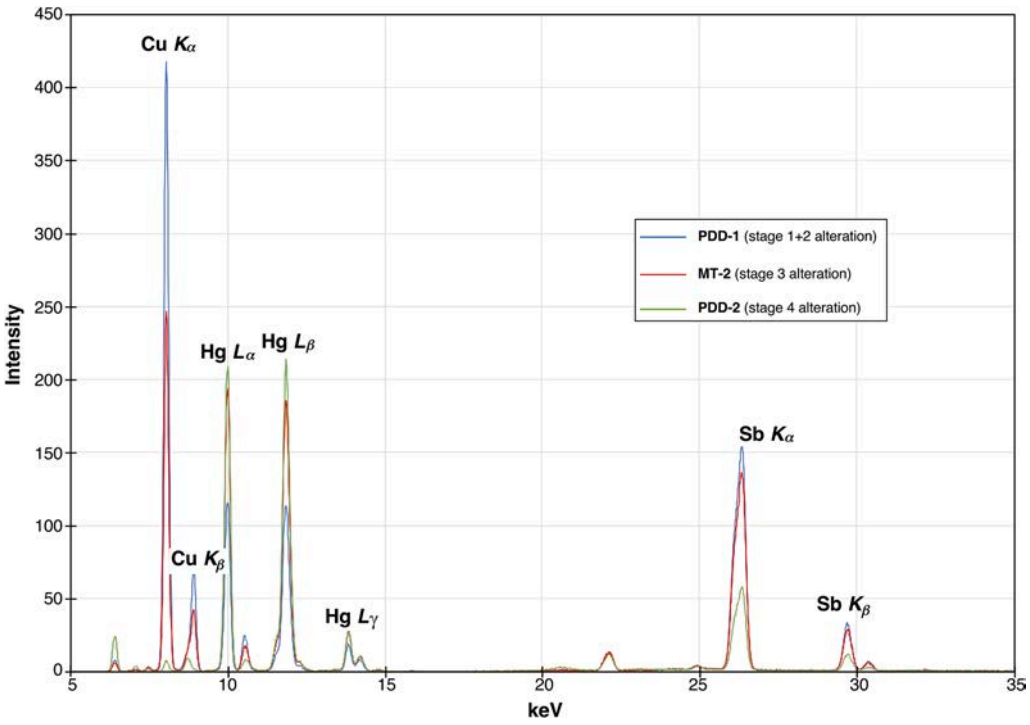

Fig. 17. HH-XRF spectra of samples PDD-1, MT-2, and PDD-2.

meteoric fluids finally completely invaded the mineralized system, favouring the genesis of the supergene minerals described in this paper.

For what concerns Type 1 FI in quartz, they allow to add further information about the post-orogenic hydrothermal circulation in the Monti Pisani area. Fig. 20 shows the different populations of fluid inclusions so far observed within vein systems of the Monti Pisani metamorphic complex.

Type 1 FI are very similar to Type IV of Dini et al. (1998) which were found in quartz vein systems from the Vorno valley (along with other minor vein systems in the areas of Sant'Andrea di Compito, Colle di Compito, and Guamo). They were interpreted as due to the interaction of metamorphic fluids with evaporitic horizons originally hosted within the phyllitic member of the Scisti Verdi belonging to the Quarziti di Monte Serra Fm. Type 1 FI observed in quartz crystals embedded in the marble of San Giuliano Terme, therefore, may represent, with Type IIa and IV FI of Dini et al. (1998) (Fig. 20), a further evidence of the occurrence of high salinity fluids in the Monti Pisani. Fluid inclusions observed in baryte closely related to the Cu-Sb-Hg mineralization are more similar to Type I, II, and III FI of Dini et al. (1998) and to the FI found in *syn*-D_1 quartz veins from Mt Cascetto (Leoni et al., 2009), interpreted as metamorphic fluids with moderate salinity. Type 2a FI are hotter and slightly more saline than those reported by these authors, but the FI association recorded the progressive dilution of these fluids through the mixing with meteoric waters. This group of FI was probably related to the *syn*-metamorphic devolatilization of the lower portions of the Santa Maria del Giudice Unit where the organic-rich Permo-Carboniferous Scisti di San Lorenzo Fm. could be a possible source of Hg for hydrothermal fluids. Although geochemical data on this formation are lacking, Baroni et al. (1994) reported some relatively high Hg contents (up to 662 ng/g) in Carboniferous rocks from Tuscany.

In summary, tetrahedrite-(Hg) from San Giuliano Terme, and associated other members of the tetrahedrite group, may be the result of the circulation of fluids dominated by a metamorphic component and characterized by moderately high T and salinity, within brittle fractures cutting the Liassic "Calcari ceroidi" Fm. This ore assemblage was later deeply altered, due to the massive ingression of meteoric water within the fractured system. The weathering of tetrahedrite-(Hg), although not temporally constrained, is probably related to the exhumation of metamorphic units during post-Miocene times. In this regard, it is worth noting that Rau and Tongiorgi (1974) described the occurrence in this area of Pliocene sediments within fractures related to normal faults, and D'Amato Avanzi and Nardi (1993) proposed a general uplift of the area immediately located NW of San Giuliano Terme starting from middle Pliocene. This could have favored the exposure and pervasive supergene weathering of the Cu-Sb-Hg mineralization described in this paper.

5.2. *Supergene weathering of tetrahedrite-(Hg) and relative mobility of its chemical constituents*

Our mineralogical and geochemical data allow us to reconstruct the processes that occurred during the weathering of tetrahedrite-(Hg) and to establish the relative mobility of its four main chemical constituents, namely Cu, Hg, Sb, and S.

Supergene mineral assemblages in the four stages document a progressive oxidation of tetrahedrite-(Hg) and the introduction into the system of Ca^{2+}, HCO_3^- and H_2O, as well as the progressive removal of S, Sb, and Cu. Meteoric waters in equilibrium with the marbles (calcite ± dolomite) of the studied area are indeed calcium-bicarbonate type (Fulignati and Sbrana, 2009).

During stage 1, the pristine TGM was exposed to the incipient infiltration of the meteoric H_2O but the oxidation was probably limited, due to the low fluid/TGM ratio. The aqueous fluid infiltrating along thread-like pathways dissolved the TGM, causing the precipitation of a Cu_2S-like phase at the fluid-TGM interface, followed by cinnabar and the RGM + malachite progressively away from the fluid-TGM interface (Fig. 11). The textural features and mineral assemblages are like those reported by Majzlan et al. (2018) for the alteration of a solid solution between tetrahedrite-(Fe) and tennantite-(Fe), the only difference being represented by the widespread occurrence of cinnabar and the absence of detectable tripuhyite in the samples from San Giuliano Terme. Mercury seems to have a high affinity with reduced S and immediately precipitates as HgS. Minor elements occurring in tetrahedrite-(Hg) (i.e., Zn, Fe, and As) have different fates. Zinc seems to be rapidly removed, as no phases containing this element have been detected. This agrees with

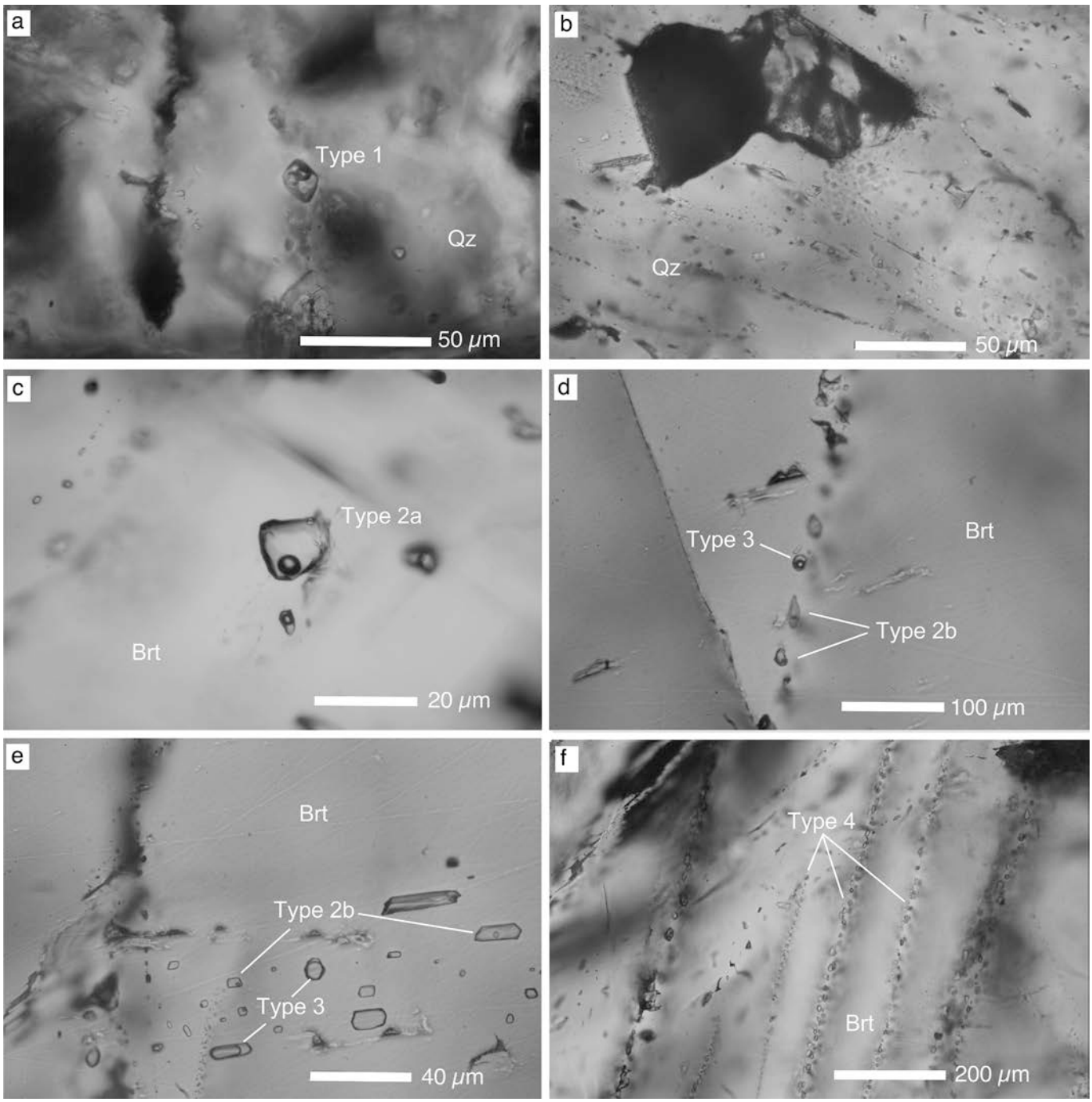

Fig. 18. Optical microscope images of the different types of fluid inclusions found in quartz and baryte crystals from San Giuliano Terme (samples SGT-3 and MT-1, respectively). a) Primary Type 1 multiphase (LVHS) fluid inclusion in quartz. b) Pseudosecondary Type 1 multiphase (LVHS) fluid inclusions in quartz. c) Primary Type 2a two-phase liquid-rich (LV) fluid inclusions in baryte. d,e) Secondary trails of Type 2b two-phase liquid-rich (LV) fluid inclusions and associated Type 3 two-phase vapor-rich (VL) fluid inclusions in baryte. f) Secondary trails of Type 4 monophase liquid only (L) fluid inclusions in baryte.

Majzlan et al. (2018) and Keim et al. (2018) who reported the rapid loss of Zn. Iron and As occur as minor elements in RGM.

In stage 2, the TGM matrix is more pervasively invaded by the aqueous fluid and the fluid/TGM ratio increases. However, during both weathering stages 1 and 2, the *p*H and fO_2 conditions should not have changed significantly because the Cu_2S-like phase is still present. During both stages, the Sb of TGM is (at least partially) oxidized from Sb^{3+} (TGM) to Sb^{5+} (RGM), Hg remains as Hg^{2+} in cinnabar, whereas Cu is partially oxidized from Cu^{+} (TGM and Cu_2S-like phase) to Cu^{2+} (malachite). Sulfur is partially preserved as S^{2-} in cinnabar and Cu_2S-like phase, and mostly oxidized to SO_4^{2-} and removed from the system as dissolved anion; the occurrence of minor baryte in association with supergene minerals could be related to this process and demonstrates the Ba mobility in the supergene environment, in agreement with Majzlan et al. (2018).

During stages 3 and 4, the fO_2 conditions became more oxidizing as reflected by the absence of Cu-sulfides and the almost complete dissolution of TGM. The original volume of TGM is now largely occupied by cinnabar and voids. Considering an initial Hg and S concentration of the pristine TGM of 17.6 wt% and 22.2 wt%, respectively (Tab. 2), and a calculated density of 5.406 g/cm^3 (based on electron microprobe analysis and unit-cell parameters determined through single-crystal X-ray

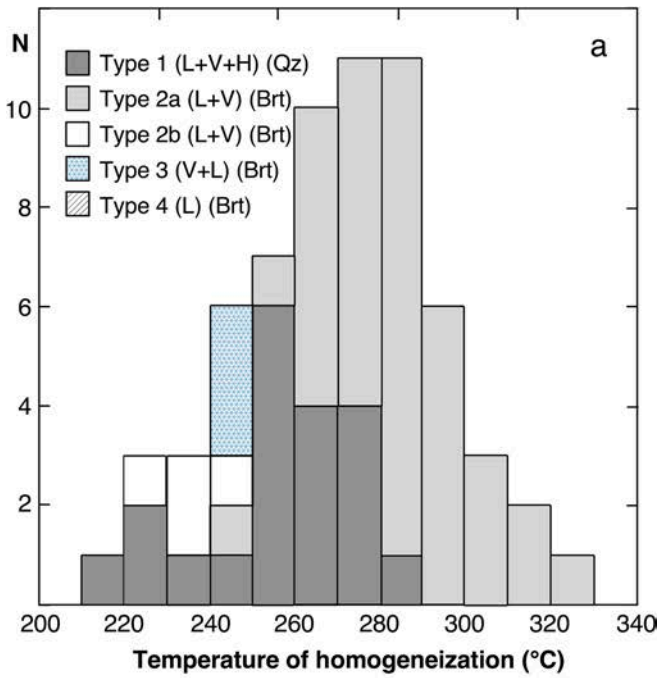

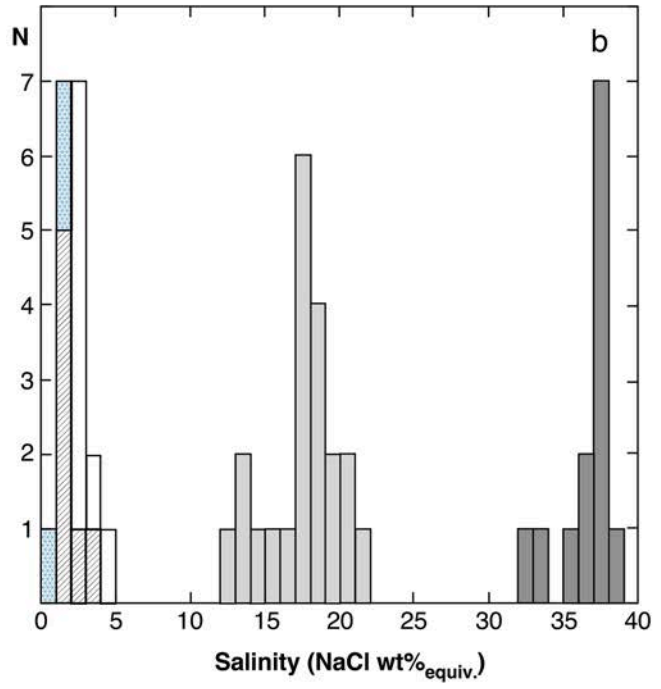

Fig. 19. Histograms of the homogenization temperatures (a) and salinities (b) of Type 1, Type 2a, Type 2b, Type 3 and Type 4 (only salinity) fluid inclusions found in quartz and baryte crystals from San Giuliano Terme (samples SGT-3 and MT-1, respectively). N = number of measurements.

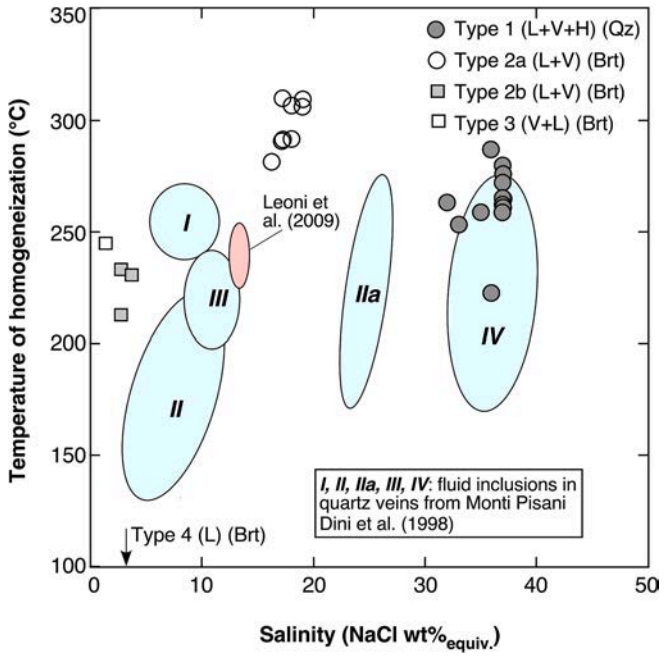

Fig. 20. T_{hom}-salinity diagram showing the different populations of fluid inclusions from the Monti Pisani metamorphic complex. Light blue and pink areas represent data after Dini et al. (1998) and Leoni et al. (2009), respectively. (For interpretation of the references to color in this figure legend, the reader is referred to the web version of this article.)

diffraction), if the initial Hg is entirely converted into cinnabar then this latter would occupy 13.5 % of the TGM volume, and 87.3 % of the initial mass of S will be lost from the system. X-ray maps of red earthy material (sample PDD-2; Fig. 16) indicate that the volume fraction of cinnabar in this material is comparable to this theoretical value, thus suggesting that Hg can be considered a virtually immobile element in the geochemical environment under consideration, precipitated as cinnabar as soon as it is liberated from the TGM during alteration.

Generally, the transition from stage 1 to stage 4 in the alteration of tetrahedrite-(Hg) is marked by an increase in the porosity and in the modal abundance of cinnabar, with a continuous change in the mineralogy of supergene phases. Moreover, one can observe the progressive migration of malachite from the inner portion of the TGM crystal towards the host rocks, infiltrating along grain boundaries and giving rise to typical green coatings on the marble surfaces. The relative mobility of Cu, Sb and Hg can be evaluated by qualitatively analysing the bulk composition of the samples PDD-1 (stage 1 + stage 2), MT-2 (stage 3) and PDD-2 (stage 4). As shown in Fig. 17, the HH-XRF spectra suggest the following relative mobility of the chemical constituents during the whole weathering process: Hg < Sb < Cu ≪ S.

This result may help in interpreting the observations of Barago et al. (2023) who studied the fate of some potentially toxic elements during the alteration of Hg-rich TGMs from the Mt Avanza ore deposit (northeastern Italy). According to these authors, Hg occurs in surprisingly low concentrations in different solid matrices (soil and sediment) as well as in water, similar to the behaviour of this element in cinnabar deposits. According to the results of our investigation, this may be due to the precipitation of cinnabar during the alteration of Hg-bearing tetrahedrite, with the consequent sequestration of Hg in a solid matrix.

6. Summary and conclusions

Mineralogical, petrographical, geochemical, and fluid-inclusion data allowed us to characterize the genesis of tetrahedrite-(Hg) and to reconstruct its supergene weathering path. As discussed by Keim et al. (2018), the phases generated during supergene weathering of TGMs are related to the composition of primary TGMs but also to several physicochemical parameters directly related to the geological environment where these processes take place.

The samples studied in this work belong to a Cu-Sb-Hg mineralization hosted in *meta*-carbonate rocks, and their genesis is due to the circulation of hydrothermal fluids of dominantly metamorphic origin and having a temperature of ~ 285 °C and a salinity of ~ 17.5 wt% $NaCl_{e.quiv.}$; the moderately high salinity of these fluids may have favoured the transport of Hg, possibly sourced in organic-rich Permo-Carboniferous

metasediments, as Hg-Cl complexes.

During post-Miocene times, tetrahedrite-(Hg) underwent a progressive oxidation and leaching, promoted by the ingression of meteoric water into the mineralized area. Ca^{2+}, HCO_3^- and H_2O were introduced into the system, whereas S, Sb, and Cu were progressively oxidized and removed. Based on mineralogical and textural features, four different stages of supergene weathering can be recognized. Textural characteristics, as well as the increasing porosity in the final stages of the alteration process, are very similar to those reported by previous authors (e.g., Borčinová Radková et al., 2017; Keim et al., 2018; Majzlan et al., 2018) for other members of the tetrahedrite group. The main difference is the massive precipitation of cinnabar, whose abundance indicates that Hg can be considered as a virtually immobile element during TGMs alteration at the considered physicochemical conditions.

This result has interesting environmental implications, as Hg is one of the priority pollutant metals commonly hosted in TGMs and its sequestration in cinnabar may preclude, or strongly reduce, its dispersion into the environment. Since different physicochemical conditions (e.g., different *p*H or Eh values) may affect the behaviour of tetrahedrite-(Hg) upon supergene weathering, conditioning the mobility of Hg, similar investigations of TGMs alteration processes from other geological settings are highly desirable to achieve a complete picture of the geochemical behaviour of Hg in the surficial environment.

Declaration of competing interest

The authors declare that they have no known competing financial interests or personal relationships that could have appeared to influence the work reported in this paper.

Data availability

Data used in the research are reported in the paper

Acknowledgements

C. Frassi, L. Pandolfi, and G. Molli are thanked for useful discussions about the geological setting of the studied area. CB and MD acknowledge financial support from the Ministero dell'Istruzione, dell'Università e della Ricerca through the project PRIN 2017 "TEOREM – deciphering geological processes using Terrestrial and Extra-terrestrial ORE Minerals", prot. 2017AK8C32. MD and AG acknowledge financial support from Pisa University's "Progetti di Ricerca di Ateneo - PRA-2020-25". The study was also financially supported by Slovak Research and Development Agency (contract No. APVV-22-0041) for JS, and by the Ministry of Culture of the Czech Republic (long-term project DKRVO 2024-2028/1.I.a; National Museum, 00023272) for ZD. The Centro per l'Integrazione della Strumentazione Scientifica dell'Università di Pisa (C.I.S.U.P.) is acknowledged for the access to the C.I.S.U.P. laboratories. We appreciate the constructive reviews by an anonymous referee and by the Associate Editor.

Appendix A. Supplementary data

Supplementary data to this article can be found online at https://doi.org/10.1016/j.oregeorev.2023.105847.

References

Atencio, D., Andrade, M.B., Christy, A.G., Gieré, R., Kartashov, P.M., 2010. The pyrochlore supergroup of minerals: nomenclature. Can. Mineral. 48, 673–698.

Balestrieri, M.L., Pandeli, E., Bigazzi, G., Carosi, R., Montomoli, C., 2011. Age and temperature constraints on metamorphism and exhumation of the syn-orogenic metamorphic complexes of Northern Apennines, Italy. Tectonophysics 509, 254–271.

Barago, N., Mastroianni, C., Pavoni, E., Floreani, F., Parisi, F., Lenaz, D., Covelli, S., 2023. Environmental impact of potentially toxic elements on soils, sediments, water, and air nearby an abandoned Hg-rich fahlore mine (Mt. Avanza, Carnic Alps, Italy). Environ. Sci. Pollut. R., doi: 10.1007/s11356-023-26629-7.

Baroni, F., Protano, G., Riccobono, F., 1994. Mercury content of the rocks of Tuscany. A geochemical contribution to geology of Hg-ores. Atti Accad. Fisiocritici Siena 15, 59–67.

Bernhardt, H.-J., Schmetzer, K., 1992. Belendorffite, a new copper amalgam dimorphous with kolymite. Neues Jb. Miner. Monat. 1992, 21–28.

Biagioni, C., George, L.L., Cook, N.J., Makovicky, E., Moëlo, Y., Pasero, M., Sejkora, J., Stanley, C.J., Welch, M.D., Bosi, F., 2020a. The tetrahedrite group: nomenclature and classification. Am. Mineral. 105 (1), 109–122.

Biagioni, C., Sejkora, J., Musetti, S., Velebil, D., Pasero, M., 2020b. Tetrahedrite-(Hg), a new 'old' member of the tetrahedrite group. Mineral. Mag. 84 (4), 584–592.

Biagioni, C., Sejkora, J., Raber, T., Roth, P., Moëlo, Y., Dolníček, Z., Pasero, M., 2021. Tennantite-(Hg), Cu6(Cu4Hg2)As4S13, a new tetrahedrite-group mineral from the Lengenbach quarry, Binn. Switzerland. Mineral. Mag. 85, 744–751.

Bodnar, R.J., 1993. Revised equation and table for determining the freezing point depression of H_2O–NaCl solutions. Geochim. Cosmochim. Acta 57, 683–684.

Borčinová Radková, A., Jamieson, H., Lalinská-Voleková, B., Majzlan, J., Števko, M., Chovan, M., 2017. Mineralogical controls on antimony and arsenic mobility during tetrahedrite-tennantite weathering at historic mine sites Špania Dolina-Piesky and L'ubietová-Svätodušná Slovakia. Am. Mineral. 102, 1091–1100.

Carnasciali, M.M., Costa, G.A., 2001. Cu_xHg_y: a puzzling compound. J. Alloy Compd. 317–318, 491–496.

Carosi, R., Leoni, L., Tamponi, M., 1992. Temperature di metamorfismo e «cristallinità» dell'illite nell'unità di S. Maria del Giudice (Monti Pisani, Appennino Settentrionale). Atti Soc. Tosc. Sci. Nat., Mem Serie A 99, 161–173.

Carosi, R., Cerbai, N., Montomoli, C., 1997. Deformation history of the Verrucano of Pisani Mounts (Northern Apennines, Italy). Annales Tectonicae 9, 55–75.

Carosi, R., Montomoli, C., Pertusati, P.C., 2002. Late orogenic structures and orogen-parallel compression in the Northern Apennines. Boll. Soc. Geol. Ital., Volume Speciale 1, 167–180.

Chi, G., Diamond, L.W., Lu, H., Lai, J., Chu, H., 2021. Common problems and pitfalls in fluid inclusion study: a review and discussion. Minerals 11 (7).

Christy, A.G., Atencio, D., 2013. Clarification of status of species in the pyrochlore supergroup. Mineral. Mag. 77, 13–20.

Christy, A.G., Gatedal, K., 2005. Extremely Pb-rich rock-forming silicates including beryllian scapolite and associated minerals in a skarn from Långban, Värmland Sweden. Mineral. Mag. 69, 995–1018.

Cipriani, C., Mazzetti, G., 1989. Kolymite (copper amalgam): report of second and third occurrences. Eur. J. Mineral. 1, 719–720.

Cipriani, C., Bernardini, G.P., Corazza, M., Mazzetti, G., Moggi, V., 1993. Reinvestigation of natural and synthetic silver amalgams. Eur. J. Mineral. 5, 903–914.

Crawford, M.L., 1981. Phase equilibria in aqueous fluid inclusions. In: Hollister, L.S., Crawford, M.L. (Eds.), Short Course in Fluid Inclusions: Application to Petrology v. 6. Mineralogical Association of Canada, 75-100.

D'Amato Avanzi, G., Nardi, I., 1993. Indizi di neotettonica nei Monti d'Oltre Serchio: faglie distensive recenti al bordo della pianura pisana e depositi ciottolosi a quota 170 metri. Boll. Soc. Geol. It. 112, 601–614.

D'Achiardi, A., 1873. Mineralogia Della Toscana Volume II, 404.

D'Achiardi, A., 1877. Miniere di mercurio in Toscana e considerazioni generali sulla genesi loro. Atti Soc. Tosc. Sci. Nat. 3, 132–149.

Darling, R.S., 1991. An extended equation to calculate NaCl contents from final clathrate melting temperatures in H_2O–CO_2–NaCl fluid inclusions: implications for P-T isochore location. Geochim. Cosmochim. Acta 55, 3869–3871.

Dini, A., Orlandi, P., Protano, G., Riccobono, F., 1998. Le vene di quarzo del complesso metamorfico dei Monti Pisani (Toscana): caratterizzazione strutturale, mineralogia ed inclusioni fluide. Atti Soc. Tosc. Sci. Nat., Mem., Serie A, 105, 113-136.

Foit Jr., F.F., Hughes, J.M., 2004. Structural variations in mercurian tetrahedrite. Am. Mineral. 89, 159–163.

Franceschelli, M., Leoni, L., Memmi, I., Puxeddu, M., 1986. Regional distribution of Al-silicates and metamorphic zonation in the low-grade Verrucano metasediments from the Northern Apennines Italy. J. Metamorph. Geol. 4, 309–321.

Franceschelli, M., Leoni, L., Memmi, I., 1989. b_0 of muscovite in low and high variance assemblages from low grade Verrucano rocks, Northern Apennines Italy. Schweiz. Miner. Petrogr. Mitteilungen 69, 107–115.

Franceschelli, M., Leoni, L., Sartori, F., 1991. Crystallinity distribution and crystallinity – b0 relationships in white K-micas of Verrucano metasediments (Northern Apennines, Italy). Schweiz. Miner. Petrogr. Mitteilungen 71, 161–167.

Franzini, M., Lezzerini, M., 1998. Le pietre dell'edilizia medievale pisana e lucchese (Toscana occidentale). 2 – I calcari selciferi del Monte Pisano. Atti Soc. Tosc. Sci. Nat., Mem Serie A 105, 1–8.

Franzini, M., Lezzerini, M., 2003. The stones of medieval buildings in Pisa and Lucca provinces (western Tuscany, Italy). 1 - The Monte Pisano marble. Eur. J. Mineral. 15, 217–224.

Fulignati, P., Sbrana, A., 2009. Idrogeochimica dei fluidi idrotermali di San Giuliano Terme (PI). Atti Soc. Tosc. Sci. Nat., Mem Serie A 114, 5–12.

George, L.L., Cook, N.L., Ciobanu, C.L., 2017. Minor and trace elements in natural tetrahedrite-tennantite: effects on element partitioning among base metal sulphides. Minerals 7 (17).

Goldstein, R.H., Reynolds, T.J., 1994. Systematics of fluid inclusions in diagenetic minerals. Society for Sedimentary Geology, Short Course 31, 1–199.

Goldstein, R.H., 2003. Petrographic analysis of fluid inclusions. In: Samson, I., Anderson, A., Marschall, D. (Eds.), Fluid inclusions analysis and interpretation. Mineralogical Association of Canada, Short Course, 32, 9-53.

Grassi, S., Carosi, R., Marroni, M., Ancora, D., 1992. Il sistema idrotermale di S. Giuliano Terme (PI): note di geologia, idrogeologia e geochimica. Boll. Soc. Geol. Ital. 111, 303–313.
Hackbarth, C.J., Petersen, U., 1984. A fractional crystallization model for the deposition of argentian tetrahedrite. Econ. Geol. 79, 448–460.
Inc, B.A., 2022. APEX4. Bruker Advanced X-ray Solutions, Madison, Wisconsin, USA.
Karanović, L., Cvetković, L., Poleti, D., Balić-Žunić, T., Makovicky, E., 2003. Structural and optical properties of schwazite from Dragodol (Serbia). Neues Jb. Miner. Monat. 2003, 503–520.
Karup-Møller, S., Makovicky, E., 2003. Exploratory studies of element substitutions in synthetic tetrahedrite. Part V Mercurian Tetrahedrite. Neues Jb. Miner. Abh. 179, 73–83.
Karup-Møller, S., Makovicky, E., 2004. Exploratory studies of the solubility of minor elements in tetrahedrite. VI. Zinc and the combined zinc-mercury and iron-mercury substitutions. Neues Jb. Miner. Monat. 2004, 508–524.
Keim, M.F., Staude, S., Marquardt, K., Bachmann, K., Opitz, J., Markl, G., 2018. Weathering of Bi-bearing tennantite. Chem. Geol. 499, 1–25.
Keith, L.H., Telliard, W.A., 1979. Priority pollutants-I. A perspective view. Environ. Sci. Technol. 13, 416–423.
Kemkin, I.V., Kemkina, R.A., 2013. Microheterogeneity of the Koupol deposit fahlores as a reflection of changing of physicochemical parameters of the ore-forming solution. J. Earth Sci. 24, 179–187.
Kovalenker, V.A., Bortnikov, N.S., 1985. Chemical composition and mineral association of sulphosalts in the precious metal deposits from different geological environment. Geol. Carpath. 36, 283–291.
Lafuente, B., Downs, R.T., Yang, H., Stone, N., 2015. The power of databases: the RRUFF project. In: Armbruster, T., Danisi, R.M. (Eds.), Highlights in Mineralogical Crystallography. Berlin, Germany, W. De Gruyter, pp. 1–30.
Leoni, L., Montomoli, C., Carosi, R., 2009. Il metamorfismo delle unità tettoniche dei Monti Pisani (Appennino Settentrionale). Atti Soc. Tosc. Sci. Nat., Mem Serie A 114, 61–73.
Majzlan, J., Kiefer, S., Herrmann, J., Števko, M., Sejkora, J., Chovan, M., Lánczos, T., Lazarov, M., Gerdes, A., Langenhorst, F., Borčinová Radková, A., Jamieson, H., Milovský, R., 2018. Synergies in elemental mobility during weathering of tetrahedrite [(Cu, Fe, Zn)12(Sb, As)4S13]: field observations, electron microscopy, isotopes of Cu, C, O, radiometric dating, and water geochemistry. Chem. Geol. 48, 1–20.
Majzlan, J., Števko, M., Herrmann, J., Lazarov, M., Wiederhold, J., 2019. Isotopic signature of Cu and Hg during weathering of tetrahedrite and chalcopyrite. Goldschmidt Abstract 2019, 2126.
Marini, F., Pandeli, E., Tongiorgi, M., Pecchioni, E., Orti, L., 2020. The Carboniferous-mid Permian succession of the Northern Apennines: new data from the Pisani Mts. inlier (Tuscany, Italy). J. Geosci. 139, 212–232.
Markova, E.A., Chernitsova, N.M., Borodaev, Y.S., Dubakina, L.S., Yushko-Zakharova, O. E., 1980. The new mineral kolymite, Cu_7Hg_6. Zap. Vses. Mineral. O-va. 109, 206–211.
Mills, S.J., Christy, A.G., Rumsey, M.S., Spratt, J., 2016. Discreditation of partzite. Eur. J. Mineral. 28, 1019–1024.
Mills, S.J., Christy, A.G., Rumsey, M.S., Spratt, J., Bittarello, E., Favreau, G., Ciriotti, M. E., Berbain, C., 2017. Hydroxyferroroméite, a new secondary weathering mineral from Oms France. Eur. J. Mineral. 29, 307–314.
Nickel, E.H., Williams, P.A., Downes, P.J., Buchert, D.E., Vaughan, D., 2007. Secondary minerals in a tennantite boxwork from the Bali Lo prospect, Ashburton Downs, Western Australia. Aust. J. Mineral. 13, 31–39.
Pouchou, J.L., Pichoir, F., 1985. "PAP" (φρZ) procedure for improved quantitative microanalysis. In: Armstrong, J.T. (Ed.), Microbeam Analysis. San Francisco Press, San Francisco.
Rau, A., Tongiorgi, M., 1974. Geologia dei Monti Pisani a sud-est della Valle del Guappero. Mem. Soc. Geol. Ital. 13, 227–408.
Roedder, E., 1984. Fluid inclusions. Rev. Mineral. 12, 644 p.
Seeliger, E., Mücke, A., 1972. Para-schachnerite, $Ag_{1.2}Hg_{0.8}$, und Schachnerite, $Ag_{1.1}Hg_{0.9}$, vom Landsberg bei Obermoschel Pfalz. Neues Jb. Miner. Abh. 117, 1–18.
Sheldrick, G.M., 2015. Crystal structure refinement with SHELXL. Acta Crystallogr. C 71, 3–8.
Staude, S., Mordhorst, T., Neumann, R., Prebeck, W., Markl, G., 2010. Compositional variation of the tennantite-tetrahedrite solid-solution series in the Schwarzwald ore district (SW Germany): the role of mineralization processes and fluid source. Mineral. Mag. 74, 309–339.
Sterner, S.M., Hall, D.L., Bodnar, R., 1988. Synthetic fluid inclusions. V. Solubility relations in the system NaCl-KCl-H_2O under vapor-saturated conditions. Geochim. Cosmochim. Acta 52, 989–1005.
Varekamp, J.C., Buseck, P.R., 1984. The speciation of mercury in hydrothermal systems, with applications to ore deposition. Geochim. Cosmochim. Acta 48, 177–185.
Vassileva, R., Atanassova, R., Kouzmanov, K., 2014. Tennantite-tetrahedrite series from the Madan Pb-Zn deposits, Central Rhodopes Bulgaria. Mineral. Petrol. 108, 515–531.
Vink, B.W., 1986. Stability relations of malachite and azurite. Mineral. Mag. 50, 41–47.
Warr, L.N., 2021. IMA-CNMNC approved mineral symbols. Mineral. Mag. 85, 291–320.
Wei, D., Xia, Y., Steadman, J.A., Xie, Z., Liu, X., Tan, Q., Bai, L., 2021. Tennantite-tetrahedrite-series minerals and related pyrite in the Nibao Carlin-type gold deposit, Guizhou SW China. Minerals 11 (2).
Wilson, A.J.C., 1992. International Tables for Crystallography. Volume C: Mathematical, Physical and Chemical Tables. Kluwer Academic Publishers, Dordrecht, The Netherlands.
Wu, P., Gu, X., Qu, K., Yang, H., Wang, Y., 2021. Argentotetrahedrite-(Hg), IMA 2020–079. CNMNC Newsletter 59. Eur. J. Mineral. 33, 139–143.
Wu, I., Petersen, U., 1977. Geochemistry of tetrahedrite and mineral zoning at Casapalca. Peru. Econ. Geol. 72, 993–1016.
Zajzon, N., Szentpéteri, K., Fehér, B., Szakáll, S., Kupi, L., Barkóczy, P., 2012. New data on Cu-amalgams, kolymite and belendorffite from Rudabánya, Hungary. Acta Mineralogica Petrographica, Abstract Series 7, 160.